NOISE REDUCTION IN THZ-TDS DIELECTRIC CHARACTERIZATION OF THIN FILMS WITH THZ INTERFEROMETRY

By

JAY A. SMALL

Bachelor of Science

University of Central Oklahoma

Edmond, Oklahoma

1997

Submitted to the Faculty of the Graduate College
of the Oklahoma State University in partial
fulfillment of the requirements for the
Degree of MASTER OF SCIENCE
December, 2004

NOISE REDUCTION IN THZ-TDS DIELECTRIC

CHARACTERIZATION OF THIN FILMS

WITH THZ INTERFEROMETRY

Thesis Approved:

R. Alan Cheville	Thesis Advisor
Albert T. Rosenberger	
Jerzy S. Krasinski	
A. Gordon Emslie	Dean of the Graduate College

TABLE OF CONTENTS

LIST OF TABLES

LIST OF FIGURES

Chapter 1

INTRODUCTION

In recent years thin film science has grown world-wide into a major area of research. Applications in coatings and synthesis of new materials for industry have resulted in tremendous increase in thin film processing technologies. Currently, this development is commensurate with breakthroughs in microelectronics, optics, and nanotechnology[1]. Films with thickness in the range of one to several microns have found an essential role in a multitude of production technologies such as thermal barrier coatings and wear protection that enhance the service life of tools and protect materials against thermal and atmospheric influences[2]. One reason for the growing significance of thin film science is the advanced development of various means of in situ film characterization such as reflection high-energy electron diffraction (RHEED), scanning probe microscopy (SPM), ellipsometry, and plasma analysis techniques.

THz Time Domain Spectroscopy

The use of time-domain THz spectroscopy has been an important tool for nearly 2 decades to measure dielectric properties of optically opaque materials that are transparent at THz frequencies3. Its application to thin film science has steadily grown in recent years. In THz-TDS a single cycle electromagnetic pulse with THz bandwidth is generated and

detected by photoconductively switching the transmitter and receiver with femtosecond laser pulses centered at 810 nm and focused onto the chip. The THz transmitter generates freely propagating pulses of THz electromagnetic radiation across bandwidths that can range from 100 GHz to 5 THz.4.

THz Generation and Detection

Generation of short THz pulses relies on the creation of transient highly-mobile free carriers in a semiconductor that undergo acceleration in the presence of a strong electric field. The semiconductor of choice is high-resistivity unimplanted gallium arsenide (GaAs) owing to electron mobility of approximately 8,000 $^{cm^{-1}}/_{V \cdot s}$ [5]. On the surface of the GaAs chip is a lithographically fabricated strip transmission line configured as shown in Figure 1. Most radiation propagates into the chip where a spherical silicon lens collects and collimates the pulse train for propagation into the rest of the measurement apparatus. The generated THz radiation is typically collimated by a silicon lens and off-axis paraboloidal mirrors.

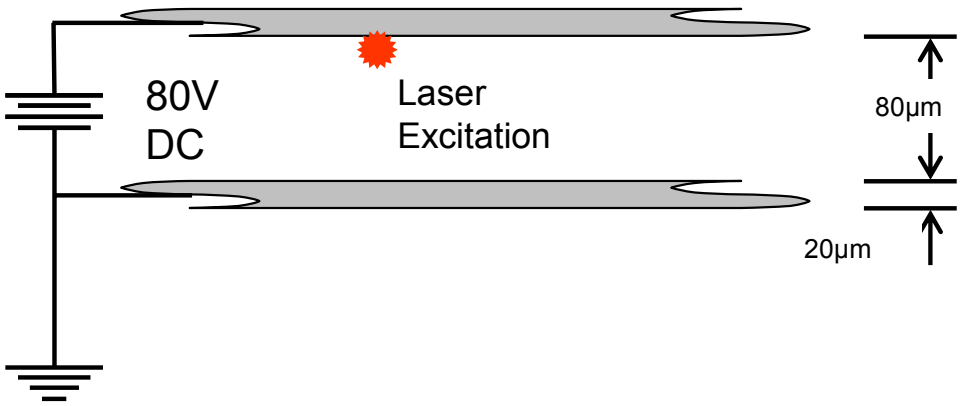

Figure 1. Coplanar strip transmission lines are lithographically fabricated on high-resistivity GaAs. The lines have the dimensions shown and are DC biased at up to 80V. Femtosecond pulses from a Ti-Sapphire mode-locked pulse laser are incident on the anode at the position shown which generate free electrons and holes which accelerate from the high electric field to produce coherent short THz pulses.

Detection of the THz pulses also relies on the response of highly mobile transient carriers to an electric field. Rather than from a manually applied field in the case of the transmitter carriers flow from that of the passing THz pulse which is tightly focused onto the detector chip made of ion implanted silicon on sapphire. Implantation reduces carrier recombination time to a few hundred femtoseconds[6]. This is essentially the sampling time of the photoconductive switch over which the electric field of the THz pulse is averaged. A variety of antenna structures have been used for THz receivers. This research uses the structure shown in Figure 2.

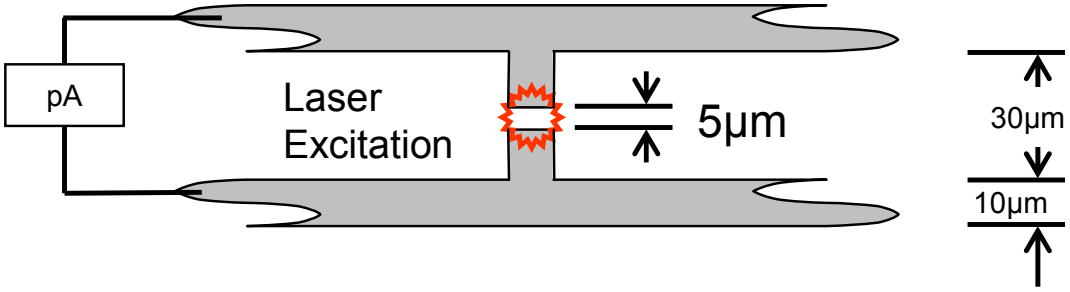

Figure 2. Dipole antenna structure of a THz receiver chip. A spherical silicon lens collects the THz pulse train and focuses it onto the chip while 100 fs optical laser pulses closes the 5μm switch with the generation of transient carriers. During the lifetime of the carriers (~100 fs) current flows according to the electric field orientation and strength of the passing THz pulse.

An antenna structure with the dimensions shown is lithographically fabricated on the silicon side of the chip. A spherical silicon lens collects the THz pulse train and focuses it onto the chip while 100fs laser pulses close the 5μm switch at a rate of approximately 90 MHz. Because the path for the optical excitation of both transmitter and receiver are fixed for any given position of an adjustable laser path length delay, the synchronization of switch-activation and pulse arrival is ensured. During the time the switch is closed current flows according to the electric field of the passing THz pulse. The current is averaged over the actuation time of the switch and results in a current that can be measured as an average

current by an ordinary ammeter. By then adjusting the arrival time of the laser pulses the electric field profile of the THz pulse is systematically recorded. In this way phase information carried on the pulses are measured directly.

Principle of Measurement Technique

The coherence length of near single-cycle THz pulses generated by photoconductive switching is on the order of 0.8 mm[7]. By passing THz pulses through a sample with complex frequency-dependent refractive index $n(\omega) = n_r(\omega) - in_i(\omega)$ the complex

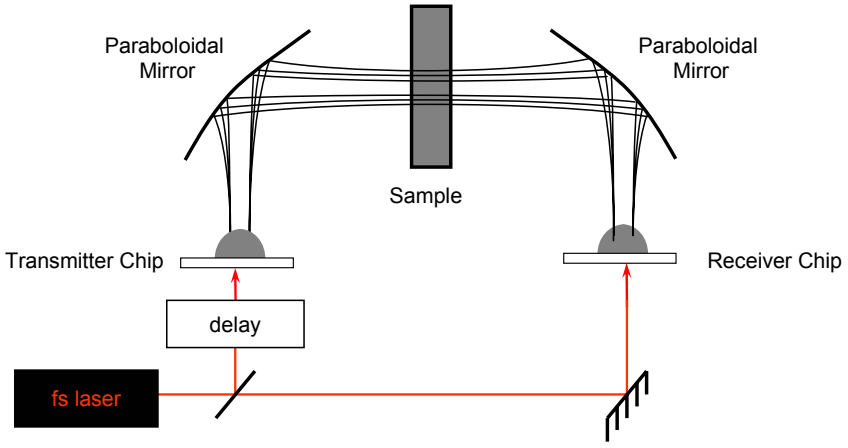

Figure 3. Schematic of a single-beam THz time domain spectroscopy system.

amplitude spectrum of the pulse returns information on the refractive index and absorption of the sample by comparing transmission through a reference. Average current data is acquired for transmission through a sample $S(t)$ and then a reference $R(t)$. The acquisition time of a 10ps scan is on the order of 3 minutes, depending upon the integration time used for phase-sensitive detection. A numerical Fourier transform of the time domain data is performed to obtain the frequency domain quantities $S(\omega)$ and $R(\omega)$. Then the ratio

$$\frac{S(\omega)}{R(\omega)} = \exp\left[-i\frac{\omega}{c}\left(n_r(\omega) - in_i(\omega) - 1\right)d\right] \qquad 1$$

with sample thickness d is used to extract the frequency-dependent refractive index $n_r(\omega)$ and absorption coefficient $\alpha(\omega) = \omega n_i(\omega)/c$ according to

$$n_r(\omega) - in_i(\omega) = i\frac{c}{\omega d}\ln\left(\frac{S(\omega)}{R(\omega)}\right) + 1. \qquad 2$$

C h a p t e r 2

MEASUREMENT LIMITS AND TREATMENT OF NOISE

Noise Sources

The contributions of noise sources in standard THz-TDS fall into one of three discrete categories[8] corresponding to noise from the emitter, detector, and all other noise contributions labeled as drift. Because each of these contribute independently of the other they are considered uncorrelated and can be expressed analytically as a square variance value σ^2 contributing together according to [9]

$$\sigma_{tot}^2 = \sigma_1^2 + \sigma_2^2 + ...\sigma_N^2 \qquad 3$$

where σ_{tot} is the total variance of the combination of independent variances $\sigma_{1,2...N}$. In a THz-TDS system the variances in the electric field between discrete THz pulses give rise to a variance in the current of the THz detector which in turn gives rise to a variance in voltage, the quantity actually measured.

In this notation the noise sources can be analytically represented as power variances[10]. We can write $\sigma^2_e(\omega)$ for the THz emitter, $\sigma^2_{sh}(\omega)$ for the shot noise in the THz detector, and $\sigma^2_d(\omega)$ for drift which refers to all other signal independent noise sources such as laser noise, electronics noise, and Johnson noise[8]. The shot noise is proportional to the electric field at the detector and can thus be written as $\sigma^2_{sh}(\omega) = 2e\Delta f X(\omega)$ with e the electron charge, Δf the

measurement bandwidth determined by the lockin integration time $1/\tau$, and $X(\omega)$ either the measured sample, $S(\omega)$ or reference, $R(\omega)$. These are obtained from numerical Fourier transforms of time domain data of the THz pulses transmitted through the sample or reference. For THz-TDS the complex transmission coefficient is represented in the notation of Duvillaret as

$$T(\omega) = \frac{S(\omega)}{R(\omega)} = \rho(\omega) e^{i\varphi(\omega)} \qquad 4$$

from which the real part of eq. 4 is extracted from the argument φ(ω) and the absorption coefficient $\alpha(\omega)$ from the modulus $\rho(\omega)$. As shown in reference 10, the dominant noise term comes from the THz emitter, $\sigma^2_e(\omega)$, especially in the case of slightly absorbing samples with $\rho(\omega)$ approaching unity, and $S(\omega) \cong R(\omega)$. For THz-TDS the sample and reference scans are measured independently and the noise on the sample and reference scans are uncorrelated. Figure 4a quantifies these noise effects where a standard TDS setup was used to show the time-evolving fluctuations measured at delay positions before and at the peak of the THz pulse shown in Figure 4b. The measurement at time delay T_1 shows an rms

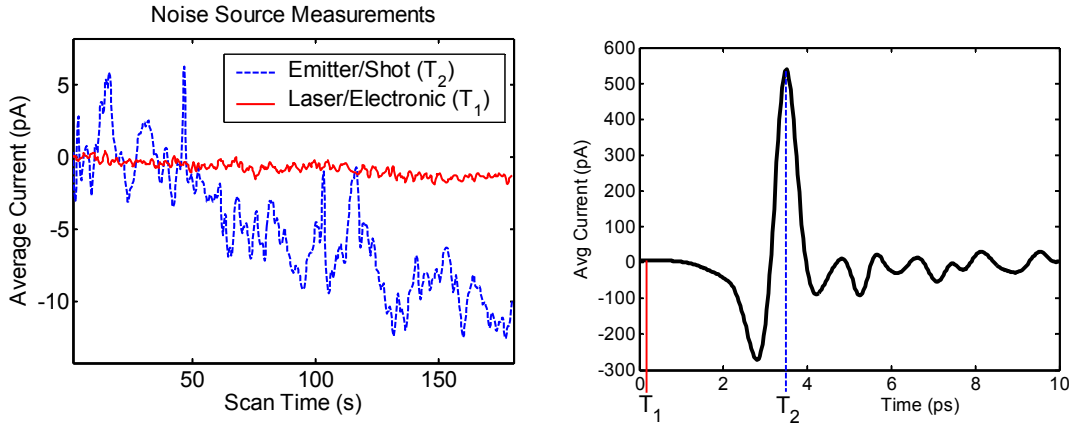

Figure 4. a) Time-evolved signal fluctuations before pulse arrival (solid) and at pulse peak (dashed). b) THz pulse in the time domain showing time delay measurement positions corresponding to the traces in figure a.

noise level of about 1 pA and represents the noise limit of the measurements system. At T_2, the pulse peak, a combined emission and shot rms noise value of $\sqrt{\sigma_e^2 + \sigma_{sh}^2} \simeq 7\,pA$ is evident as well as a system drift of $\sigma_d = 10\,pA$ over the course of a single scan.

Errors in the measurement of $n(\omega)$ are proportional to the variance of the modulus, $\sigma_\rho(\omega)$, which in turn is related to the variance of the reference, $\sigma_R(\omega)$, and sample, $\sigma_S(\omega)$, data scans[10]:

$$\sigma_\rho^2(\omega) = \frac{\sigma_S^2(\omega)}{\left|R(\omega)\right|^2} + \frac{\rho^2(\omega)}{\left|R(\omega)\right|^2}\sigma_R^2(\omega) \qquad 5$$

As in the case here $\sigma_S^2 \cong \sigma_R^2 = \sigma_{TDS}^2$ and when $\rho(\omega)$ approaches unity in the case of low index materials:

$$\sigma_\rho^2(\omega) = \frac{2\sigma_{TDS}^2(\omega)}{\left|R(\omega)\right|^2}. \qquad 6$$

Noise contributions on the sample or reference scans are then expressed as[10]:

$$\sigma_{TDS}^2(\omega) = \rho^2(\omega)\sigma_e^2(\omega) + \sigma_{sh}^2(\omega) + \sigma_d^2(\omega)$$

$$\lim_{\rho(\omega)\to 1}\sigma_{TDS}^2(\omega) = \sigma_e^2(\omega) + \sigma_{sh}^2(\omega) + \sigma_d^2(\omega) \qquad 7$$

where $\rho(\omega) \cong 1$ for a thin sample.

In a single THz-TDS data scan $R(t)$ the signal to noise ratio is often reported as high as 10,000:1[11]. This figure compares the peak signal to that measured prior to pulse arrival. However the dielectric characterization of a material requires a minimum of two THz-TDS data scans that have noise contributions uncorrelated. While each of these independently have very high signal-to-noise values the characterization measurement can be significantly affected by noise sources within the system owing to the relationship of the data to the

dielectric function of eq. 2. There it is seen that as $S(\omega)/R(\omega)$ approaches unity the quantity being measured begins to vanish. Such is the case for thin materials or those with very low index which have very little effect on the THz pulse compared to the reference. In this case $S(\omega) \cong R(\omega)$ and the measurement demands signal differences between sample and reference that are on the order of the noise sources in a THz-TDS system. For this reason a more detailed examination of these sources and their nature is of great interest in thin film research. It is also a great challenge for THz-TDS since the film thicknesses are much smaller than the wavelengths of the pulse composition.

Double-Beam Methods

By correlating the noise between the signals $S(\omega)$ and $R(\omega)$ significant measurement noise can be reduced. One method often used in IR spectroscopy involving broad bandwidth and complex spectra is double-beam in time configurations owing to the noise filtering benefits of phase-sensitive detection. Typically double-beam configurations divert the probe beam between a sample and reference path at a modulation frequency into a single phase-sensitive detector[12]. In a THz-TDS system however, there is limited path length due to the low brightness of the radiation and therefore the preference of a confocal configuration for optimal power transfer.

An immediate solution for an equivalent double-beam experiment is to modulate the sample itself in and out of a single THz beam within a confocal system. Known as differential time domain spectroscopy (DTDS), this technique has been done and used to determine the refractive index of a 300 nm thick parylene-N film[13] and other thin or low

index films[13, 14]. For short THz pulses if the sample is homogeneous, uniformly flat and mountable on a substrate or can in some other way be modulated between reference and sample + reference, small differences in reference and sample measurements can be discriminated through phase-sensitive detection. While THz-TDS becomes problematic when $S(t)-R(t)$ is small, in DTDS time domain data of the difference between sample and reference $D(t)=S(t)-R(t)$ is obtained rather than $S(t)$ and $R(t)$ alone. $D(t)$ is measured for each position of optical delay $z=ct$ at the modulation frequency so that

$$\sigma^2_{DTDS}(t) < \sigma^2_{TDS}(t) \qquad 8$$

owing to the shorter measurement time $(1/f_{\mathrm{mod}})$ between the fields $S(t)$ and $R(t)$. Compared to several minutes for $S(t)$ and $R(t)$ when measured in the separate scans of TDS, DTDS substantially reduces noise associated with system fluctuations that occur on the time scale of a TDS measurement[15]. As with any THz time domain spectroscopy technique $R(t)$ must also be obtained in a separate scan in order to characterize dielectric properties. For DTDS instead of eq. 1 for THz-TDS the ratio $\mathrm{D}(\omega)/R(\omega)$ is used. For the case of a free-standing sample or modulation of the index itself of a sample with negligible absorption the refractive index is given by[14]

$$n(\omega)=\sqrt{\frac{2c}{\omega d}\left|\frac{D(\omega)}{R(\omega)}\right|+1} \qquad 9$$

with substantially increased sensitivity over standard THz-TDS. The primary limitation of DTDS is homogeneity of the sample and substrate since surface features are averaged out due to modulation. By using a double modulation technique in which both the sample and the THz beam itself are modulated and measured using two lock-in amplifiers films as thin

as 100nm have been characterized[15].

Interferometry

Electromagnetic radiation is an electric and magnetic field oscillating in space with field amplitude and phase propagating at the speed of light. The majority of electromagnetic detection devices such as photodiodes and photo multiplier tubes measure energy which is proportional to the square of the magnitude of electric field, intensity, and independent of their phase of oscillation. Information about phase interaction is therefore lost with intensity measurement alone. Some techniques such as ellipsometry measure intensity but capitalize on polarization-dependent interactions of light with matter which renders intensity proportionate to phase.

Interferometry is another highly successful technique that correlates frequency-

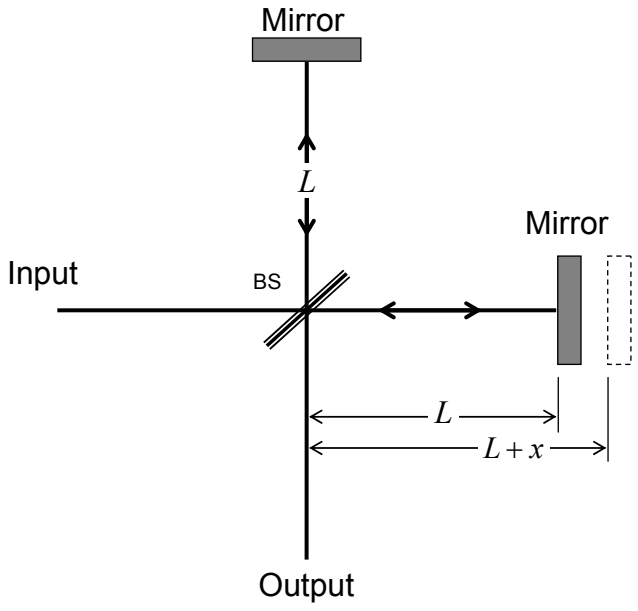

Figure 5. One example of interferometry.

specific electric field amplitude and phase with intensity. Numerous configurations exist, however, all of them are based on a controlled difference in propagation distance between two beams of light to vary the relative phase between them. An example of an interferometer is shown in Figure 5 where a single beam of wavelength λ is split by beam splitter (BS) into two beams that traverse 2*L* and 2(*L*+*x*). When recombined at BS their phase differs by $\frac{2\pi}{\lambda}2x$. Since the output beam is described by

$$E_{out} = E_0\left(1+e^{i\frac{2\pi}{\lambda}x}\right) \qquad 10$$

the intensity attains maximum when $x = n\frac{\lambda}{2}$ and minimum for $x = (2n+1)\frac{\lambda}{4}$ for *n*=0,1,2…

IR Interferometry

The most common and widely successful use of interferometry in the far IR band is infrared Fourier transform (FT-IR) owing to the availability of IR sources with broad spectral content and at a wavelength scale that affords convenient instrumentation. Fourier Transform Spectroscopy in general has applications from 10 cm^{-1} to 10,000 cm^{-1}. An FT-IR technique uses a broad-band IR source such as a mercury arc lamp that emits from 2 to 15 THz. Filters are often used to isolate bands of interest. Referring to Figure 6, an IR beam is directed into a Michelson interferometer which has one arm fixed at length *D* and the other of variable

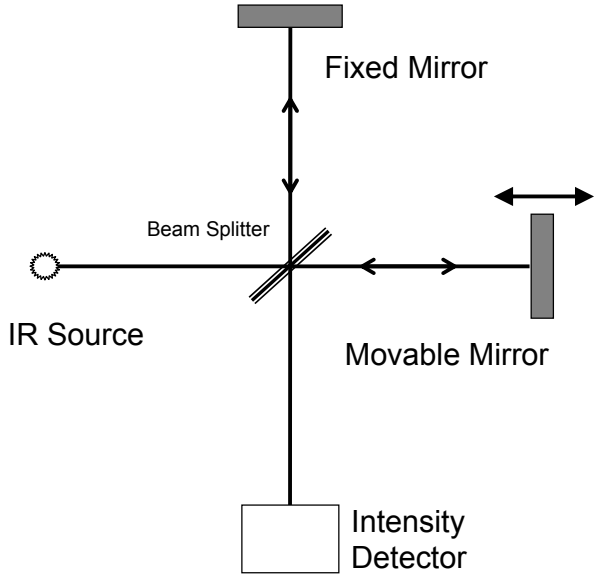

Figure 6. Schematic of an FT-IR Spectrometer.

length d on a high-precision translation stage. The movable arm is calibrated so that the equidistant position $D=d$ is precisely known as well as all points along the translation direction. Incident radiation is split at the beam splitter where light undergoes phase propagation $\exp\left(ik\left(\lambda\right)2d+i\phi\right)$ and $\exp\left(ik\left(\lambda\right)2D+i\phi\right)$ for the movable and fixed arms, respectively. An arbitrary phase factor ϕ is the phase at the first pass of the beam splitter. The beams traverse the arms then recombine at the splitter after which the intensity is generally measured. However, at the splitter the two beams differ in phase by

$$\Delta\left(\lambda\right)=\frac{2\pi}{\lambda}2\left(D-d\right). \qquad 11$$

Wavelengths with phase difference 2π add constructively while all others add destructively. From eq. 11 for any wavelength constructive interference can only occur when

$$D-d=n\frac{\lambda}{2}. \qquad 12$$

Thus there is a direct correlation between the position of the movable arm and the spectral content of the intensity measurement at each position *d*. The spectral content is usually restricted to $n=1$ to avoid spectral overlap. An FT-IR interferogram is a measure of intensity as a function of arm length difference. Because the interaction between the arms is dependent on the phase of the electric fields and *not* intensity the interferogram reports phase information across the frequency sweep. The spectral content is obtained by a numerical Fourier transform of the interferogram. Because FT-IR provides phase information the complex dielectric constant of a sample can be extracted.

THz-TDS Interferometry

In principle THz-TDS interferometry is a spectroscopic technique that can be done with many of the known interferometric configurations used at other spectral regions. For THz-TDS the motivation for interferometry differs on two primary fronts from that of intensity-measuring interferometers. First, the typical interest in interferometry is the access to phase information using relatively simple sensors which measure intensity, not phase. THz-TDS on the other hand already provides phase information at IR frequencies with a higher signal to noise than for interferometry using thermal detectors[12]. Thus, on the basis of phase information THz interferometry would be redundant. However, the fundamental motivation for THz-TDS interferometry is to reduce noise in phase measurements of THz-TDS. The mechanism of noise reduction will be thoroughly discussed in later sections but the point is emphasized here that the motivation for THz interferometry is fundamentally different than spectrally similar techniques such as FT-IR.

Because traditional THz-TDS measures transmission changes in a broadband

spectrum, it is difficult to accurately characterize materials when the sample is thin, of low differential index, or highly absorptive materials which must be made thin to permit transmission. As the interaction effects of the sample become small by either low refractive index or diminishing sample thickness, $S(\omega) \cong R(\omega)$ and characterization measurements become proportionate to the noise levels in the measurement system.

As discussed previously, DTDS is effective at increasing noise rejection for high quality samples owing to lockin detection of $S(\omega) - R(\omega)$. Some thin samples, however, are not practical to modulate such as liquids or free-standing films. In these cases the noise reduction benefits of THz time domain interferometry provides a solution[7, 16, 17].

In research done prior to this work THz-TDS interferometry is based on achieving complete destructive interference of the output signal of a Michelson-type interferometer. This relies on the provision that one arm of the interferometer induces a phase shift $\Phi(\omega) = \pi$ across the entire bandwidth of coherent THz pulses. A frequency-dependent phase shift has been attained by reference [7] through the Gouy phase shift and by reflections from a metallized face on one of two silicon right-angle prisms in reference 16.

In THz interferometry if $R(\omega)$ and $S(\omega)$ denote signals in the reference and sample arms independently and $E_{meas}(\omega)$ is the interferometric measurement $R(\omega)+S(\omega)$, eq. 2 is modified[16] to include residual field $E_{\Phi}(\omega)$ that results from non-ideal cancellation between $R(\omega)$ and $S(\omega)$. Thus, to characterize the complex refractive index of a sample using THz interferometry the index is obtained from

$$n_r(\omega) - in_i(\omega) = -i\frac{c}{\omega d}\ln\left[\frac{E_{meas}(\omega) - E_{\Phi}(\omega)}{E_{\Phi}(\omega) - R(\omega)} + 1\right] + 1. \qquad 13$$

Three data scans must be obtained: $E_{meas}(\omega)$, $R(\omega)$, and $E_{\Phi}(\omega)$[16]. This has been done

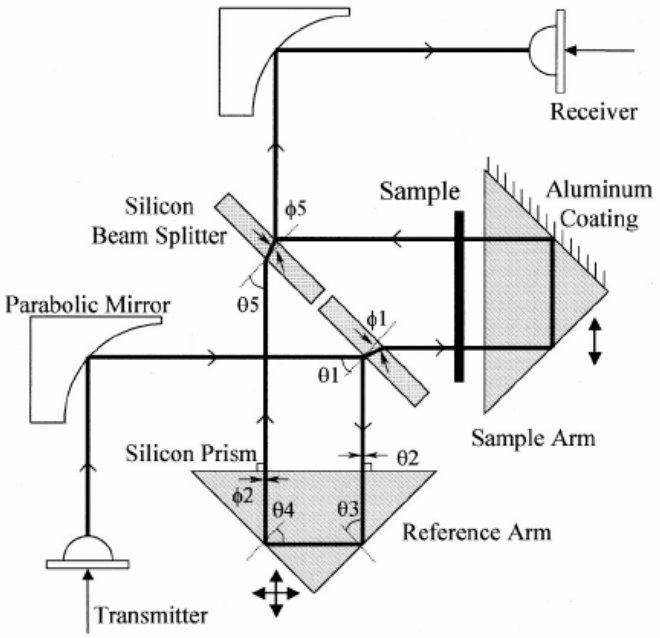

Figure 7. Reprint of the THz Michelson interferometer used in reference 16 to characterize a free standing Mylar film and oxide layers of silicon.

in previous work where results have been obtained through a variety of THz-TDS interferometry scenarios to demonstrate the resolution of the technique. Other researchers have measured free standing Mylar® films, and oxide layers of silicon[16] using the interferometer configuration of Figure 7. In the case of Mylar® a 2 μm free-standing film was suspended in the sample arm and characterized with THz Interferometry. The corresponding resolution of the measurement with $n_{Mylar}(\omega) = 1.67$ is an optical path length change of $3.34\mu m$ per pass through the sample. The extracted frequency-dependent refractive index using eq. 13 is shown in Figure 8 which shows good agreement across the frequency range of the THz pulses indicated between shaded regions. Other interferometric configuration have been used in THz imaging techniques in which a sample acts as a reflecting surface and compared to an optical flat[18].

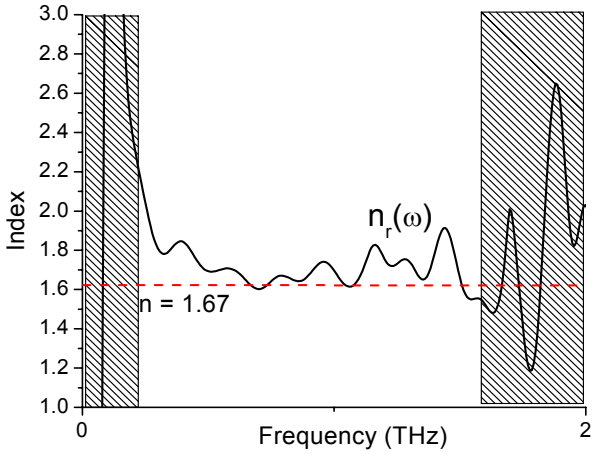

Figure 8. Reprint of the real refractive index for 2μm thick Mylar film measured by reference 16 using the THz interferometer of Figure 7.

C h a p t e r 3

THEORY

THz Michelson Interferometer

Because the radiation of the THz pulses is coherent the analytical representation of the fields in matrix notation is most suited to Jones polarization analysis, since the alternative Mueller notation describes only incoherent sources where polarization can be a mixture[19]. Thus, with the complex input field $\mathbf{E}_i(\omega)$ from the transmitter written as

$$\mathbf{E}_i(\omega) = E_{i_x}(\omega)\hat{\mathbf{x}} + E_{i_y}(\omega)\hat{\mathbf{y}},$$

the Jones matrix form is

$$\underset{\sim}{\mathbf{E}}_i(\omega) = \begin{bmatrix} E_{i_x}(\omega) \\ E_{i_y}(\omega) \end{bmatrix}. \qquad 14$$

Here and in the following treatment the underscore tilde (~) denotes a matrix. In the case of a fully linearly *x*-polarized input field such that $E_{i_y}(\omega) = 0$ and $E_i(\omega) = E_{i_x}(\omega)$ eq. 14 reduces to

$$\underset{\sim}{\mathbf{E}}_i(\omega) = \begin{bmatrix} 1 \\ 0 \end{bmatrix} E_i(\omega). \qquad 15$$

In reality, the polarization content of THz pulses emitted with the configuration used is not purely linear[20]. Furthermore, some cross polarization is expected due to off-axis

illumination of the paraboloidal mirror. However one may obtain linear polarization to within measurable limits with the insertion of a free-standing wire grid oriented to transmit the primary field and block the secondary one subsequent to the first paraboloidal mirror. Such polarizers have been used extensively in THz spectroscopy[21, 22, 23, 24].

In the context of the incident field described by eq. 15 the complex field at the receiver is calculated using the Jones matrix representation of the internal optical elements of the interferometer assuming ideal frequency-independent elements. For a sample of thickness d and wave constant $\boldsymbol{k}$, $\underset{\sim}{M}_1$ is the matrix representation of the first off-axis paraboloidal mirror, $\underset{\sim}{P}_1$ a linearly polarizing wire-grid polarizer. $\underset{\sim}{B}_t$ and $\underset{\sim}{B}_r$ are respectively the silicon beam splitter under transmission or reflection, both of which occur for each arm. $\underset{\sim}{S}_0$ and $\underset{\sim}{S}$ are the reference and sample materials. $\underset{\sim}{R}_A$ and $\underset{\sim}{R}_B$ are roof mirrors A and B while $\underset{\sim}{M}_2$ is the second paraboloidal mirror. No cross-polarization occurs after reflection from $\underset{\sim}{M}_2$ because the beam is coaxially incident to the paraboloidal mirror[25]. By establishing a complex frequency-dependent factor $\tilde{\kappa}(\omega)$ accounting for the reflection losses according to the Fresnel relations resulting from the silicon beam splitter the polarization terms are separated from the loss terms. Here $\tilde{\kappa}(\omega)$ omits terms corresponding to multiple reflections since the beam splitter is thick enough to place them outside the time domain of analysis. See Appendix D for complete development of $\tilde{\kappa}(\omega)$.

The emerging polarized field at the receiver to be calculated according to

$$\mathbf{E}_{out} = \left[\tfrac{1}{2}\underset{\sim}{M}_2\left(\underset{\sim}{B}_r\underset{\sim}{R}_A\underset{\sim}{S}_0\underset{\sim}{B}_t + \underset{\sim}{B}_t\underset{\sim}{R}_B\underset{\sim}{S}\underset{\sim}{B}_r\right)\underset{\sim}{P}_1\underset{\sim}{M}_1\right]\mathbf{E}_i(\omega)\tilde{\kappa}(\omega). \qquad 16$$

Here the quantity in brackets reduces to a single 2×2 operator matrix $\underset{\sim}{T}$ representing passage of an input pulse through *both* arms of the interferometer so that eq. 16 can be

more compactly written as

$$\mathbf{E}_{out}(\omega) = \underset{\sim}{T}\mathbf{E}_i(\omega)\tilde{\kappa}(\omega) \qquad 17$$

with

$$\underset{\sim}{T} = \tfrac{1}{2}\underset{\sim}{M}_2\left(\underset{\sim}{B}_r\underset{\sim}{R}_A\underset{\sim}{S}_0\underset{\sim}{B}_t + \underset{\sim}{B}_t\underset{\sim}{R}_B\underset{\sim}{S}\underset{\sim}{B}_r\right)\underset{\sim}{P}_1\underset{\sim}{M}_1. \qquad 18$$

Evaluation of eq. 18 by substituting the standard matrix operators for each of the defined elements yields

$$\underset{\sim}{T} = \frac{1}{2}\begin{bmatrix} e^{ik(\omega)2d} - e^{ik_0(\omega)2d} & 0 \\ 0 & 0 \end{bmatrix}. \qquad 19$$

where *2d* in the exponential terms arise due to the THz pulses traveling twice through the sample. See Appendix A for complete development of $\underset{\sim}{T}$.

Using this with eq. 15 we find that

$$\mathbf{E}_{out}(\omega) = \frac{1}{2}\begin{bmatrix} e^{ik(\omega)2d} - e^{ik_0(\omega)2d} & 0 \\ 0 & 0 \end{bmatrix}\begin{bmatrix} 1 \\ 0 \end{bmatrix}\mathbf{E}_i(\omega)\tilde{\kappa}(\omega)$$

and finally

$$\mathbf{E}_{meas}(\omega) = \mathbf{E}_{out}(\omega) = \frac{1}{2}\left(e^{ik(\omega)2d} - e^{ik_0(\omega)2d}\right)E_i(\omega)\tilde{\kappa}(\omega)\hat{\mathbf{x}}. \qquad 20$$

As verification we see from eq. 20 that in the absence of a sample d=0 and the null signal occurs at the output regardless of the orientation of $\mathbf{E}_i(\omega)$.

Noise Reduction by THz Interferometry

To compare the effects of noise on sample characterization using THz-TDS and THz interferometry the noise contributions are analyzed for the later using frequency dependent spectral amplitudes $S(\omega)$ and $R(\omega)$. For THz interferometry, rather than eq. 7 of ref 10 a

more relevant noise figure is derived based on the measured interference signal $D(\omega) = R(\omega) + S(\omega)$. For thin samples $R(\omega) \simeq -S(\omega)$ owing to the π phase shift between each arm of the interferometer. Since in THz interferometry the difference is obtained for each pulse, the emitter noise is correlated between the sample and reference arms. Thus, a similar expression to eq. 7 developed by Duvillaret for TDS can be derived for the noise content for the extraction of index in an interferometric measurement $\sigma_{int}(\omega)$:

$$\sigma_{int}(\omega) = \left\{ \left[1 - \rho(\omega)\right]^2 \sigma_e^2(\omega) + \sigma_{sh}^2 \left[R(\omega) - S(\omega) \right] + \sigma_d^2(\omega) \right\}^{1/2}. \qquad 21$$

As before $\sigma^2_{e}(\omega)$ is the THz emitter noise, $\sigma^2_{sh}(\omega)$ the THz detector shot noise and $\sigma^2_{d}(\omega)$ is long term system drift—all other signal independent noise sources such as laser noise, electronic noise, and Johnson noise[8, 10]. Because

$$S(\omega) = \rho(\omega) R(\omega)$$

we can write eq. 21 as

$$\sigma_{int}^2(\omega) = \left[1 - \rho(\omega)\right]^2 \sigma_e^2(\omega) + \sigma_{sh}^2 \left[1 - \rho(\omega)\right] + \sigma_d^2(\omega) \qquad 22$$

for a complete interferometric extraction of $n(\omega)$. For $k(\omega)d << 1$, the modulus of the difference signal, $1-\rho(\omega)$, is proportional to $\left| \frac{\omega d n(\omega)}{c} R(\omega) \right|$ in the case of transparent, $n'(\omega) \gg n''(\omega)$, or lossy, $n'(\omega) \ll n''(\omega)$, samples[16]. In the thin sample limit eq. 22 becomes

$$\lim_{\rho(\omega) \to 1} \sigma_{int}^2(\omega) = \sigma_d^2(\omega) \qquad 23$$

where it is seen that the dominant noise sources[8], emitter and shot noise tend to vanish for thin films.

Duvillaret has experimentally shown that $\sigma_d^2(\omega)$ is three orders of magnitude smaller than the combined effects of $\sigma_e^2(\omega)+\sigma_{sh}^2(\omega)$ in THz-TDS systems[10]. With this result the uncertainty of extracted index $\Delta n(\omega)$ can be compared between THz interferometry and THz-TDS by eqs. 23 and 7:

$$\frac{\Delta n(\omega)_{int}}{\Delta n(\omega)_{TDS}} \propto \sqrt{\frac{\sigma_d^2}{\sigma_e^2+\sigma_{sh}^2+\sigma_d^2}} \simeq \frac{1}{30}. \qquad 24$$

Thus, we conclude that for thin films THz interferometry reduces uncertainty in measurement of dielectric constants by a factor of 30.

The previous analysis assumes ideal cancellation of the two arms of the interferometer; in an actual experiment interferometer interference of the sample and reference pulses can achieve approximately 98% amplitude cancellation possibly due to lack of rotational symmetry of the THz beam[16, 20]. THz beam asymmetry could represent the fundamental limitation in the Michelson interferometer and is not explicitly considered in the preceding analysis. Actual improvements due to absence of this artifact have yet to be verified.

However, with ideal beam cross sectional symmetry power in the THz beam is uniformly symmetric about the vertical reflection plane and the fields uniformly cancel in the absence of a sample to produce the null field at the receiver. Measurements confirm that power transmission is not uniformly symmetric across the beam which would logically result in residual fields after recombination even under ideal optical alignment[20]. Figure 9 is an example of data published by Reiten et.al clearly illustrating the condition. Since the Michelson interferometer design relies on a π phase shift, essentially a reflection between the outputs of each arm to achieve complete destructive interference, the cross section of

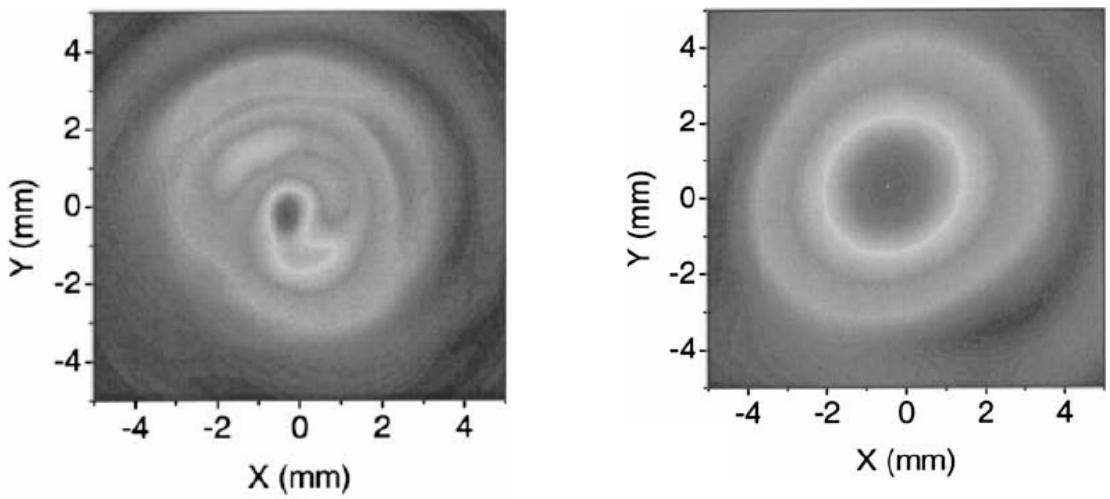

Figure 9. Data taken from reference 20 which show electric field amplitude distributions for 0.58 THz (left) and 0.18 THz (right). The asymmetry of the beam cross section is evident and is the source of rotational asymmetry mismatch noise resulting in non-zero cancellation signal in the Michelson interferometer when no sample is present.

one arm is at best an identical mirror image of the other across a reflection plane defined by the roof mirror. Consequently the overlapping of asymmetric field cross sections contains regions of small but non-trivial residual fields whose effects appear in the non-zero maximum-cancellation signal as seen in Figure 10.

The impact of this artifact arises in that the maximum-cancellation signal must be included for the extraction of refractive index of a sample. This is in addition to the typical reference scan with the sample arm blocked and a sample scan with the sample arm open. The noise contribution is two fold. The additional scan adds to the overall time required for the measurement increasing the effects of laser drift. Additionally, the stability of the maximum-cancellation signal follows the stability of the beam cross section, with the time-evolved degree of symmetry a possibly significant noise source. When the interaction effects of a sample are very small this stability is an important factor depending on the rate of symmetry fluctuation. In the previous section asymmetry effects and any fluctuation in asymmetry is included in overall drift terms and THz interferometry has shown to

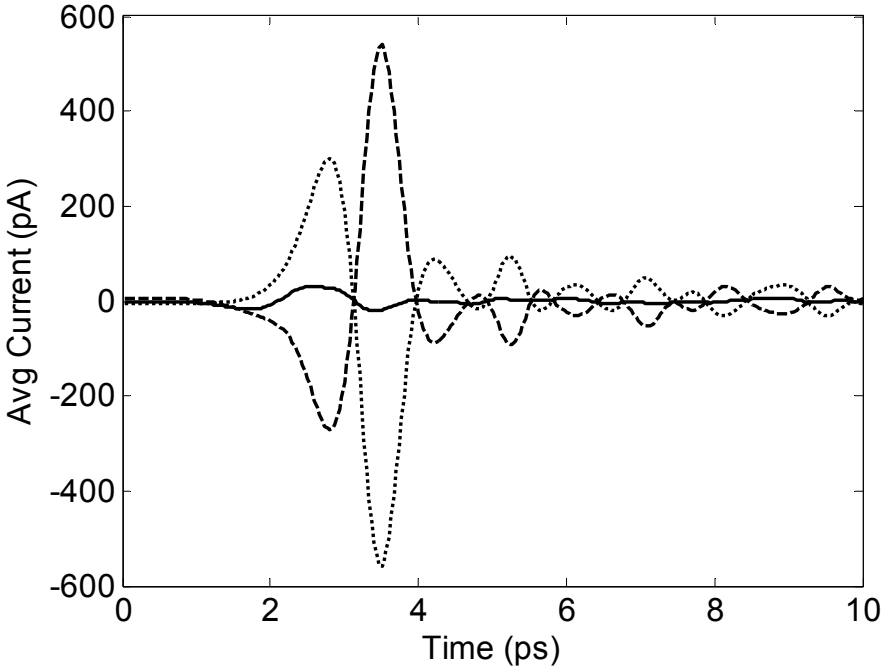

Figure 10. Time domain measurements using the Michelson interferometer with no sample in place. Dashed and dotted are with each the reference and sample arm blocked. Solid is the interference measurement showing a peak to peak cancellation of %2.6 of the arms measured independently possibly owing to beam asymmetry effects.

effectively neutralize this noise source. Nonetheless, if noise effects from beam asymmetry issue can be brought under further control, the additional noise reduction could render the reference cancellation signal experimentally negligible.

Interferometer Characterization

Tilted Dielectric Slab

In neutralizing the effects of dominant noise sources, the capabilities of THz TDS are extended so that thinner dielectric materials can be characterized using THz interferometry. We are thus interested in experimentally measuring the smallest change in

optical path length that can be accurately resolved with the technique. This requires a systematic method in measuring changes in optical path length (ΔOPL) withstanding two conditions:

1) ΔOPL must be controllable with a high degree of precision.
2) ΔOPL must be known independently of the measurement beyond the resolution of THz interferometry.

One experimental method that meets these criteria is based on rotation of a plane-parallel dielectric slab in which precise rotation of the slab results in precise knowledge of the resulting ΔOPL . However, despite the geometric simplicity of the plane-parallel slab and the fact that rotation displacement is known to within 0.001°, this characterization technique is not as experimentally trivial as it may first appear. A number of geometrical subtleties govern the optimal configuration of the tilted-slab technique in order to assure precise knowledge of ΔOPL . They arise because of the experimental difficulty of initially aligning the slab so that the THz beam is normally incident to a precision that will satisfy condition 2). The normal-incidence setup is done by minimizing the arrival time of THz pulses reflecting from the face of the slab. However, for THz pulse resolution of ¼ ps and a propagation length of .251m this allows an alignment resolution of only 1.4° . As a consequence uncertainty is associated with the actual incident angle at normal and therefore other incident angles. This in turn introduces uncertainty in the independent knowledge of ΔOPL which may violate condition 2).

With first attempts to conduct measurements using the tilted slab the magnitude this effect was not fully appreciated. Initial measurements of ΔOPL were naively attempted with path changes relative to normal incidence. Rotations yielding predicted ΔOPL in the

range of 500nm returned wildly unpredictable data. Additional measures were taken to increase the precision of normal incidence by copropagating a 1500nm diode laser through the THz beam path but with no improvement. Reasonable results were finally obtained by taking the reference measurement 4° away from 0.000° according to the rotation stage controller. The reasoning was that any small error in alignment would strongly dominate a 0° incidence while less so at larger angles by some proportion. However, the thinking was that the angle must be small enough to maintain a small interference signal since this is the basis of noise reduction by THz interferometry.

Subsequent analysis presented here which carefully explores the dynamics of this technique results in determining the optimal process for best satisfying conditions 1) and 2) above. We need first to define the coordinate system to be used. Beginning with $\hat{\mathbf{k}}$, the propagation vector of the incident beam has incident angle ψ_i relative to the vector $\hat{\mathbf{N}}$ normal to the plane-parallel slab. In this coordinate system $\hat{\mathbf{k}}$ is written as

$$\hat{\mathbf{k}} = \theta\hat{\boldsymbol{\theta}} + \phi\hat{\boldsymbol{\varphi}} . \qquad 25$$

Figure 11a illustrates the coordinate system where angles θ and ϕ are positive. The system is defined such that if the beam is aligned exactly at normal incidence then

$$\hat{\mathbf{k}} = \hat{\mathbf{N}} \equiv 0\hat{\boldsymbol{\theta}} + 0\hat{\boldsymbol{\varphi}} \qquad 26$$

and $\psi_i = 0$. Next we see from Figure 11a that ψ_i in terms of θ and ϕ can be written as

$$\psi_i(\theta,\phi) = arc\cos\left[\cos(\theta)\cos(\phi)\right]. \qquad 27$$

In practice the slab's normal-incidence orientation will deviate from exactly normal by a small angle ψ_{error} which from eq. 27 can be written in terms of small error angles θ_{error} and ϕ_{error} illustrated in Figure 11b. As discussed earlier $|\psi_{error}| \le 1.4°$ which

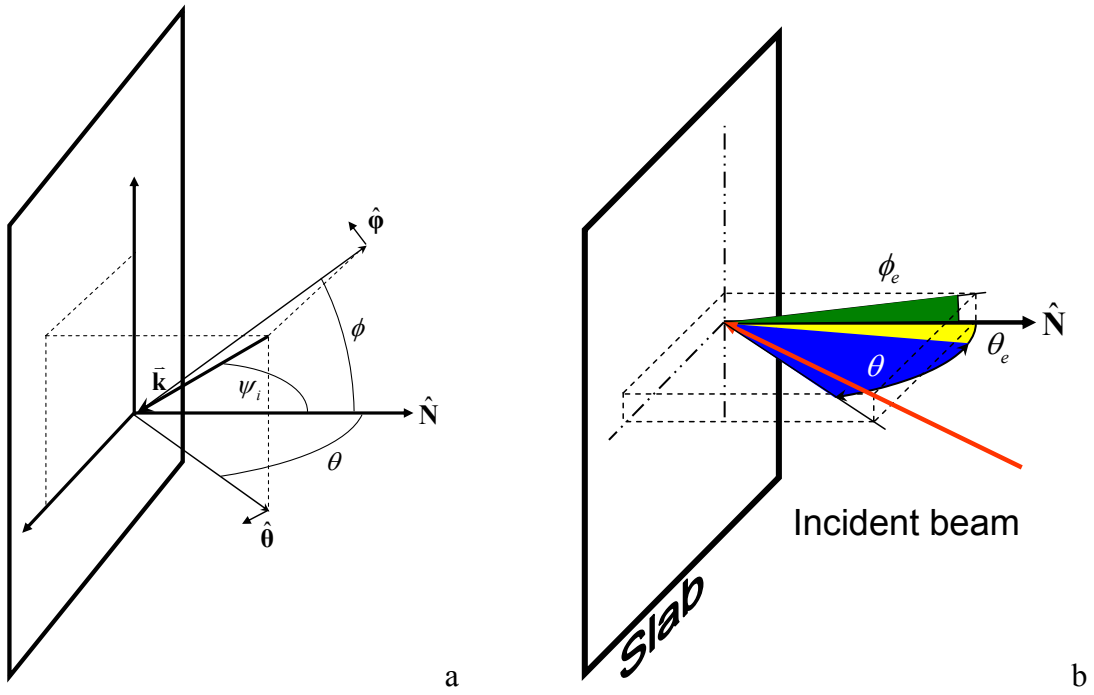

Figure 11. a) Coordinate system of tilted slab analysis. b) Illustration of error in alignment of the dielectric slab.

corresponds to $\sqrt{\phi_{error}^2+\theta_{error}^2}\le 1.4°$. The expression for change in optical path length ΔL_{OP} as a function of two unique incident angles ψ_{i_0} and ψ_{i_1} is

$$\Delta L_{OP}\left(\psi_{i_0},\psi_{i_1},d\right)=\frac{d}{\cos\left(\psi_{t_1}\right)\cos\left(\psi_{t_0}\right)}\left[\begin{array}{c} n\left(\cos\left(\psi_{t_1}\right)-\cos\left(\psi_{t_0}\right)\right)-\cos\left(\psi_{t_1}\right)\cos\left(\psi_{t_0}-\psi_{i_0}\right) \\ +\cos\left(\psi_{t_0}\right)\cos\left(\psi_{i_1}-\psi_{t_1}\right)\end{array}\right] \quad 28$$

(See Appendix E for derivation) where d is the slab thickness. ψ_{i_0} and ψ_{i_1} correspond incident angles at reference position θ_0 and displacement position θ_1, respectively, which are varied by the high-precision controller. Because $\theta_{error}\neq 0$ and $\phi_{error}\neq 0$ we have the condition $\psi_{i_0}\neq\theta_0$ and $\psi_{i_1}\neq\theta_1$. ψ_{t_0} and ψ_{t_1} are the transmission angles inside the slab according to Snell's law associated with ψ_{i_0} and ψ_{i_1}, respectively. Although they are respective functions of ψ_{i_0} and ψ_{i_1} they are left in this form for readability. Finally, n is the refractive index of the dielectric slab and because the slab is suspended in air $n_{air}=1.0$ is

substituted *a priori*.

In satisfying condition 1) eqs. 27 and 28 are used to produce the plots in Figure 12 which illustrates the dependency of ΔOPL on the choice of θ_0 and $\Delta\theta = \theta_1 - \theta_0$. In Figure 12a and Figure 12c the surface plot is drawn for initial angles near and far from zero, respectively. In Figure 12b and Figure 12d plots of specific values of θ_0 vs ΔOPL show large sensitivity increases of ΔOPL with increasing initial angle where the scale of Figure 12d is two orders of magnitude smaller than that of Figure 12b. It is evident from Figure 12d that when the start angle is large, such as the Brewster angle of 73.4° the sensitivity is

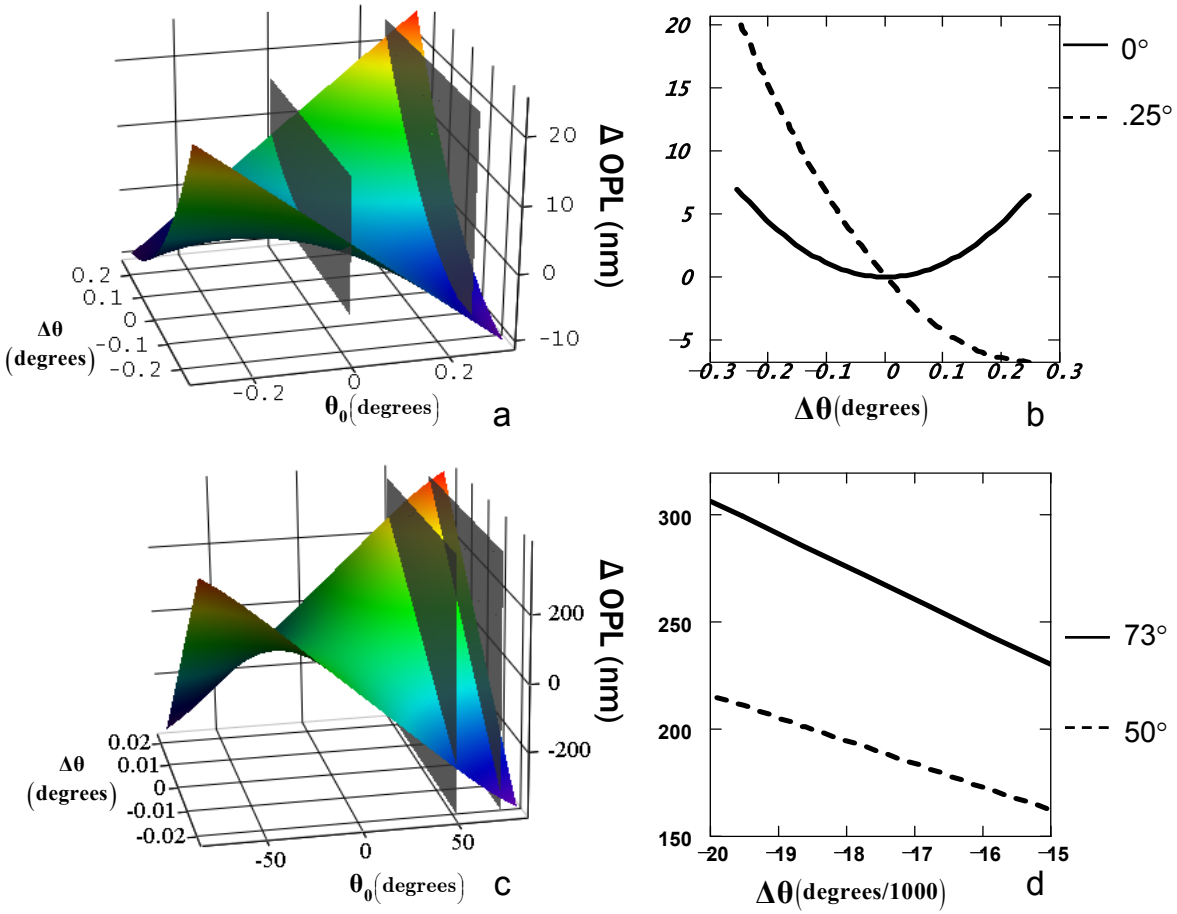

Figure 12. a) Optical path length change as a function of starting angle and displacement angle. b) OPL change for starting angle 0° (solid line) and 0.25° (dashed line). c) same as in a but for large-angle reference positions. d) same as in b but for reference positions at 50° (dotted line), and 73.4° (dash dotted line).

3 orders of magnitude greater than for initial positions taken at normal incidence and corresponds to a rate of change in ΔOPL of $\sim 16nm \pm 2nm / 0.001°$. This is half the measurable ΔOPL projected from some experimental results shown in later sections for unity SNR. Thus, Brewster angle operation appears to be near the limit of an acceptable precision of ΔOPL. In an actual experiment, smaller reference positions can be chosen to increase resolution at the expense of throughput and certainty of ΔOPL.

To satisfy condition 2) we must quantify the effect that θ_{error} and ϕ_{error} have on the knowledge of ΔOPL. Understanding the ultimate result is aided by first showing the effect that the error angles have on the path lengths at θ_0 and θ_1 independently. As developed in Appendix E, the change in optical path for arbitrary angle θ_i relative to normal incidence regardless of alignment errors is

$$D(\theta_i) = d\left[\frac{n}{\cos\left(\theta_t^{\theta_i}\right)} - n + 1 - \left(\frac{\cos\left(\theta_i - \theta_t^{\theta_i}\right)}{\cos\left(\theta_t^{\theta_i}\right)}\right)\right] \qquad 29$$

where $\theta_t^{\theta_i}$ is the angle of transmission from air into the silicon slab according to the Fresnel relations and the superscript denotes dependency on θ_i. The expression is the change in optical path length relative to exactly normal incidence with any alignment error ψ_{error} treated by $D(\theta_i + \psi_{error})$. In this way the effect of ψ_{error} on each of θ_0 and θ_1 can be examined.

Because the tilted slab technique measures ΔOPL due to changes in only θ the components θ_{error} and ϕ_{error} of ψ_{error} do not perturb the knowledge of ΔOPL by equal proportion. This is evident by plotting for θ_0 and θ_1 the error in ΔOPL as a function of

θ_{error} and ϕ_{error}. This is done with the use eq. 27 where we write θ_i in terms of θ_{error} and ϕ_{error}:

$$\theta_i\left(\theta_0+\theta_{error},\phi_{error}\right)=arc\cos\left[\cos\left(\theta_0+\theta_{error}\right)\cos\left(\phi_{error}\right)\right]. \qquad 30$$

This is then used in eq. 29 to describe the absolute error in optical path L_{err} at each position:

$$\begin{aligned} L_{err}\left(\theta_0+\theta_{err},\phi_{err}\right)&=D\left(\theta_0+\theta_{err},\phi_{err}\right)-D\left(\theta_0\right)\\ L_{err}\left(\theta_1+\theta_{err},\phi_{err}\right)&=D\left(\theta_1+\theta_{err},\phi_{err}\right)-D\left(\theta_1\right). \end{aligned} \qquad 31$$

This is plotted in Figure 13a for positions $\theta_0=0$ and $\theta_1=1.49°$ corresponding to an expected ΔOPL of $240nm$ between these positions. Clearly ϕ_{error} has nontrivial influence on the certainty of each position. However, in the tilted-slab experiment the actual quantity being measured is not the independent positions but rather

$$\Delta L_{OP}=D\left(\theta_1+\theta_{err},\phi_{err}\right)-D\left(\theta_0+\theta_{err},\phi_{err}\right). \qquad 32$$

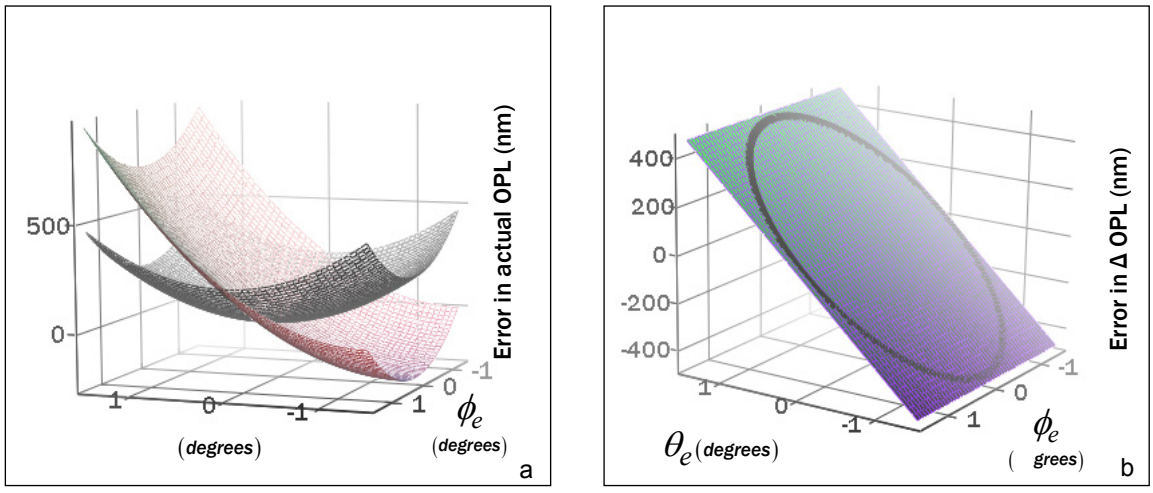

Figure 13. a) Error in the absolute optical path length for positions at 0° (gray surface) and 1.49° (red surface) as a function of the error component angles. b) The difference between the two surfaces of a) which indicates the error in the knowledge of ΔOPL. The expected ΔOPL between the two positions is 240nm. Line indicates slab alignment precision boundary of 1.4°.

Because of this the absolute error in optical path length change $\Delta L_{OP_{err}}$ in rotating from θ_0 to θ_1 is from eq. 31:

$$\Delta L_{OP_{err}}\left(\theta_0,\theta_1,\theta_{err},\phi_{err}\right)=L_{err}\left(\theta_1+\theta_{err},\phi_{err}\right)-L_{err}\left(\theta_0+\theta_{err},\phi_{err}\right). \qquad 33$$

This is plotted in Figure 13b which is the difference between the curves of Figure 13a. It is evident that the effect of ϕ_{error} is much less than that of θ_{error}. While it can be shown that

$$\frac{\partial \Delta L_{OP_{err}}}{\partial \phi_{error}} \neq 0 \qquad 34$$

and thus, the effect of ϕ_{error} does not strictly vanish, it remains within 1 nm for the region of interest.

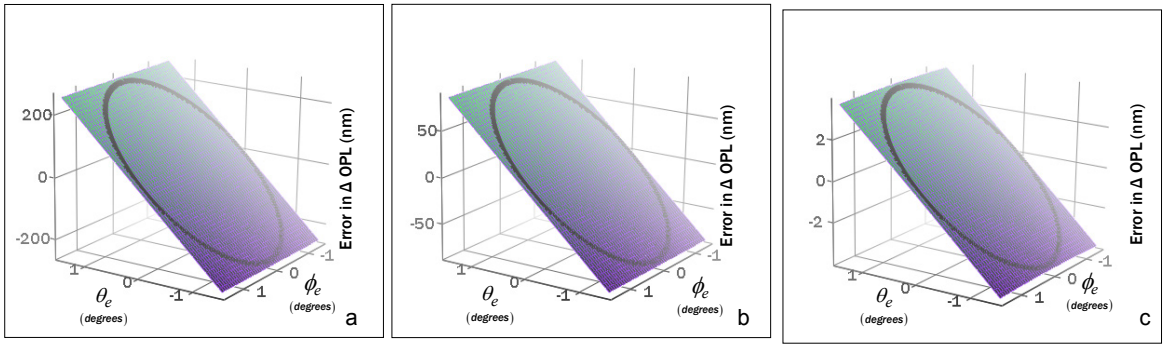

Figure 14. Error in the independent knowledge of expected ΔOPL=240 *nm* as a function of error component angles for select values of initial position. a) 1°, b) 4°, and c) 73.4°. Line indicates slab alignment precision boundary of 1.4°.

Other combinations of θ_0 and θ_1 which result in $\Delta OPL = 240nm$ are shown in Figure 14a, Figure 14b, and Figure 14c corresponding to θ_0 equal to 1°, 4°, and 73.4°. The dark line indicates the boundary for normal-incidence uncertainty angle $\psi_{error} = 1.40°$. Any of the error values inside the boundary are possible since θ_{error} and ϕ_{error} are unknown. For small θ_0, Figure 13a (0°) and Figure 14a (1°), the error is likely to be greater than the quantity being measured, violating condition 2). If θ_0 is offset by just 4° (Figure 14c) the

uncertainty magnitude is most likely around 50*nm*. In actual measurements the offset value was very near this at $\theta_0 = 3.923°$. It was selected, however, based on a rudimental understanding of the effects of θ_{error} and ϕ_{error}. Had $\theta_0 = 73.4°$ been selected (Figure 14d), Brewster's angle for silicon at THz frequencies, the error in the knowledge of ΔOPL would have been far below the expected resolution of the THz interferometer, satisfying well condition 2). Choosing the Brewster angle has another advantage of providing the highest throughput possible with this technique. Since the THz pulses travel twice through the slab upon entering and exiting the interferometer arm, the recovered reflection losses result in twice the peak signal compared to $\theta_0 = 4°$.

In conclusion, the resolution limit of THz interferometry can be successfully measured by comparing the optical path length change between two angles of incidence onto a plane-parallel dielectric slab. The technique is limited, however, by precise knowledge of path length difference independent of the measurement. The limited THz pulse width restricts the certainty of normal-incidence to only 1.4°, which has been shown to have a large effect or a negligible effect on the certainty of optical path length difference depending on the incident angles used. Measurements of a 240*nm* change involving incident angles near zero have been theoretically shown to greatly dominate the measurement by hundreds of *nm*, while for large incident angles the error is only a few *nm.* Also shown is the highly selective sensitivity in the control of path length difference which may vary by several orders of magnitude. Furthermore, enhanced throughput has been realized by choosing an incident angle at the Brewster angle where the slab is fully transparent. Thus, for a 1mm silicon slab this represents the optimal initial path for interferometer characterization for an expected optical path length change on the order

250*nm*. In such a case, the displacement angle is calculated at 0.020°, well within the precision of the rotation stage, and the errors associated with alignment of the slab are two orders of magnitude lower than the expected resolution of THz interferometry. While actual measurements of optical path length change, shown in the next chapter, were made with reference position at 3.923° rather than the more optimal Brewster angle, agreement between data and this theoretical development are within 20*nm*.

Photo-induced Index Change

Another THz interferometric experiment was carried out aimed at measuring its resolution limits with the advantage of reduced geometric complexity issues compared to the tilted slab. In this experiment photo generated free carriers in a high-resistivity silicon slab are controlled to vary the refractive index of the slab itself. This eliminates uncertainty issues associated with the orientation of the sample in the tilted slab measurements. On the other hand, independent knowledge of the actual index change is not precisely known as in the case for the tilted slab. However, since only one fitting parameter is required the technique is well-suited for interferometric characterization.

According to the Drude model the frequency dependent refractive index $n(\omega) = \sqrt{\varepsilon_r(\omega)}$ is described by [26]:

$$\varepsilon_r(\omega) = \varepsilon_\infty - \sum_{j=e,h} \frac{\omega_p^2}{\omega(\omega + i\Gamma_j)} \qquad 35$$

where $\varepsilon_\infty = 11.7$ is the relative background permittivity of Si, ω_p is the electron or hole plasma frequency given by

$$\omega_p^2 = \frac{Ne^2}{\varepsilon_0 m_{e,h}^*} \qquad 36$$

with free-space permittivity ε_0. The carrier density N is assumed equal for electrons and holes, and effective masses are taken as $m_e^* = 0.26m_e$ and $m_h^* = 0.37\ m_e$ [27]. Γ_j is the carrier damping rate $1/\tau_{e,h}$ [26]. For the > 10 kΩ–cm Si sample, the only appreciable contributions to the free carrier density are those carriers generated by optical excitation. Uniform carrier density across the sample is assumed since the measured carrier recombination time of τ_r = 25 ms (see Appendix B for measurement data) corresponds to a diffusion length L_p greater than 2mm at low carrier densities according to [28]:

$$L_p = \sqrt{\frac{kT\mu_e\tau_r}{e}} \qquad 37$$

where k is Boltzman's constant, μ_e an estimated value of the carrier mobility of 1600 $cm^2/V \cdot s$ taken from reference [27], and e the electron charge. The change of index $\Delta n(\omega)$ corresponds to the change in optical path length ΔL_{OP} reflected in measurement data according to

$$\Delta L_{OP}(\omega) = d\,\Delta n(\omega) \qquad 38$$

where d is the thickness of the silicon wafer.

Chapter 4

RESULTS

Tilted Dielectric Slab

In this work the experimental setup is that of a THz Michelson interferometer[17] consisting of a THz-TDS system configured as shown in Figure 15. THz emission has been discussed in Chapter 1. A 1.0 mm thick n-type high resistivity (> 10 kΩ-cm) silicon slab is used as a beam splitter to divide the THz beam into E_A and E_B pulse trains[16]. Front-surface,

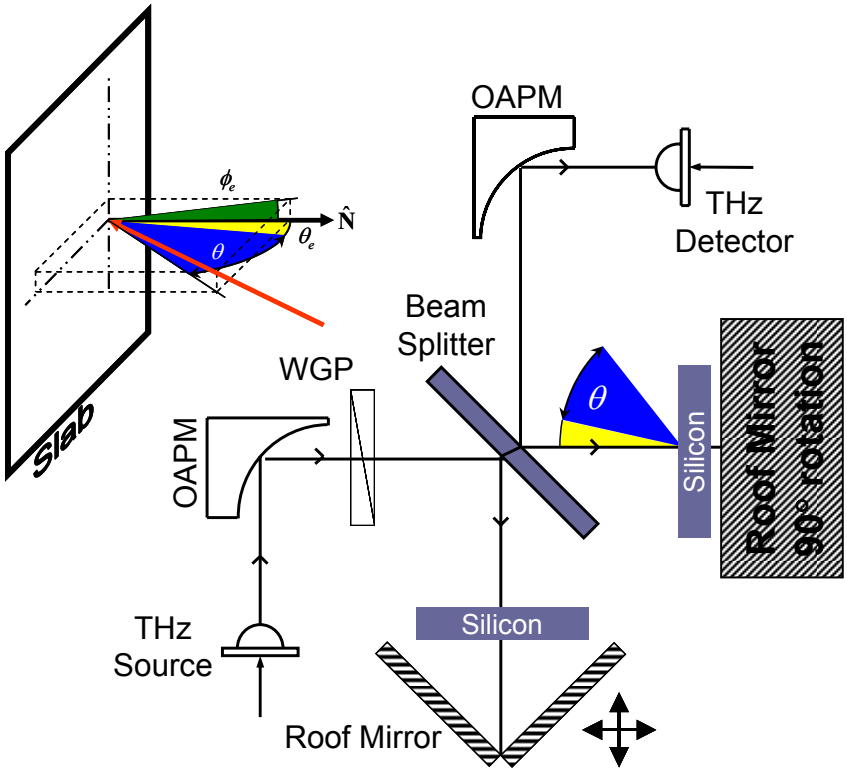

Figure 15. The THz Michelson interferometer used in the tilted slab characterization measurement.

aluminum-coated roof reflectors, labeled A and B in Figure 15 are oriented such that the incident THz beam is P-polarized at reflector A and S-polarized at reflector B. The P-polarized beam undergoes a frequency independent π phase shift due to rotation of the electric field during reflection. The pulse detected by the THz detector is thus a superposition of the pulse in the reference arm B and the π phase-shifted pulse traversing the sample arm A.

Measurements were then taken with the Michelson interferometer setup of Figure 15 with a high-precision rotational motion controller supporting a 1.0 mm n-type high resistivity (> 10 kΩ-cm) silicon slab. The orientation of the slab was set as close to normal as possible first by minimizing the arrival time of the THz pulse and subsequently by copropagating 1500nm diode laser through an estimated THz beam path. The silicon optics are transparent at this wavelength, therefore alignment throughout the system is visually aided assuming the laser is coaxial to the THz emission pattern.

Initial measurements were attempted with the reference path through normal incidence where the interferometer signal was minimized by balancing the optical path length of each arm via a translation stage. Then data was acquired before and after rotation through a displacement angle. For reasons discussed in the theory section the uncertainty in the normal incidence position of the slab resulted in highly unpredictable results. At the time of measurement the dynamics involved were not completely clear, but the normal-incidence uncertainty was suspect. By reasoning that small errors would dominate normal incidence more than other angles θ_o was set to an arbitrarily small angle of 3.923°. Results were greatly improved and data was collected for displacement angles of -.50°, -0.75°, $-1.50°$, and $-1.75°$ relative to 3.923°.

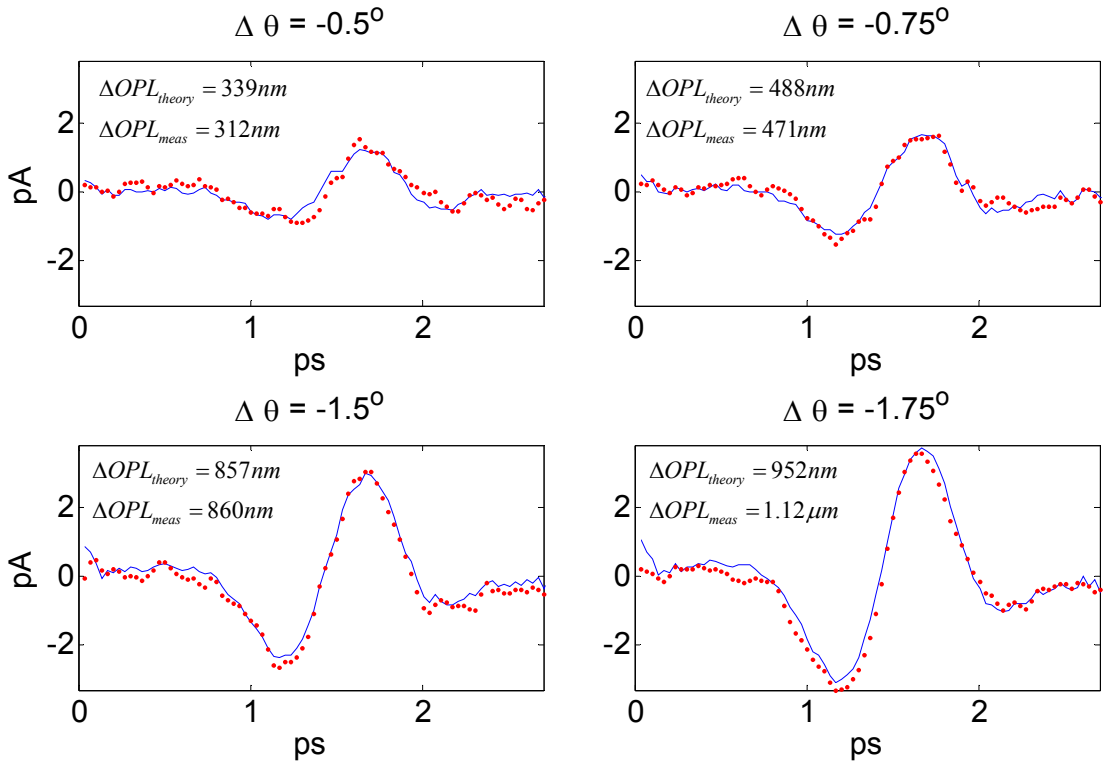

Figure 16. Interferograms of a tilted 1 mm silicon slab. In all measurements the reference path was taken at 3.923° and displacement angles are indicated. Lines represent theory where the uncertainty of normal incidence is a parameter fit to data represented by dots.

The data is shown in Figure 16 represented by dots. The quantity ΔOPL_{theory} is calculated neglecting θ_{error} and ϕ_{error}. Theoretical results shown by lines account for θ_{error} and ϕ_{error} and were numerically fit to the data through least squares iterative agreement then used to calculate ΔOPL_{meas}. The parameter values θ_{error} returned for $\Delta\theta$ values of -.50°, -0.75°, -1,50° and $-1.75°$ were -0.75°, -.59°, $-0.46°$, and +0.02°, respectively. In all cases for ϕ_{error} the value returned was less than +0.01°. From the theoretical discussion in Chapter 3 this result it not surprising, since the error resulting from ϕ_{error} changes very slightly for a 4° offset. Essentially ϕ_{error} has been rendered negligible.

The results for θ_{error} are also suggestive that aligning the slab with the copropagating diode laser may allow a better certainty than the 1.4° predicted by THz pulse arrival-time

minimization. With the exception of $\Delta\theta = -1.75°$ the consistency of parameter θ_{error} is quite good considering a standard deviation of only .145°. However, in light of the theory discussion regarding the tilted slab experiment, the measurements could be carried out in such a way as to neglect θ_{error} as well since it has been concluded that the uncertainty in ΔOPL can be mitigated to less than $\pm 5nm$.

Photo-induced Index Change

In the photo-induced refractive index change experiment the material to be characterized were 1.00*mm* thick, double side polished, > 10kΩ cm silicon wafers, arranged in each arm as shown in Figure 17. A wafer in one arm is illuminated by a cw HeNe laser (632.8 nm) incident near the Brewster angle of 76°. The fluence incident on the silicon wafer is controlled using a variable attenuator, measured with a calibrated power meter. For two primary reasons the number density of carriers *N* which take part in the measurement is not precisely known. First is that the intensity across the boundary of THz beam spot is non-uniform owing to the large incidence angle of the excitation source. Secondly, the Fresnel transmission coefficient varies across the THz spot because the excitation beam is highly divergent upon exiting the optical cable and so gives rise to non-uniform carrier generation efficiency. *N* is therefore used as the fitting parameter which directly affects the refractive index according to eqs. 35 and 36. To establish an order of magnitude estimate of the intensity at the THz beam spot the intensity was calculated accounting for non-uniformity in both the intensity and carrier generation efficiency resulting in about 2×10^{-2} mW/cm^2. The free carrier density $N = 1.96\times10^{13}$ cm^{-3} was found

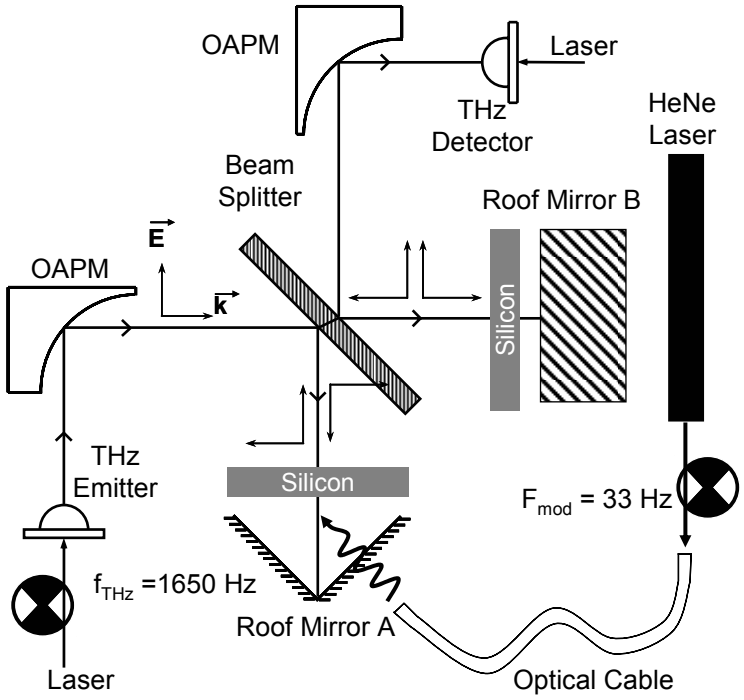

Figure 17. Photo-induced index shift experimental schematic.

by least squares iterative agreement to the data presented here and is a factor of 10 above the intrinsic carrier density.

For comparison DTDS and standard TDS measurements were performed in the same setup with the reference arm of the interferometer blocked. In DTDS the incident HeNe beam is modulated by an optical chopper at f_{mod} = 33Hz, just below $1/\tau_r$, and two lockin amplifiers are used to enhance signal to noise[29]. The first lockin amplifier has reference frequency of f_{THz} and an integration time of 1 ms and is used to measure the incident THz pulse. The output from the first lockin is sent to a second lockin amplifier with reference frequency f_{mod} and 1 s integration time that is used to detect the optically-induced change in transmission of the THz pulse.

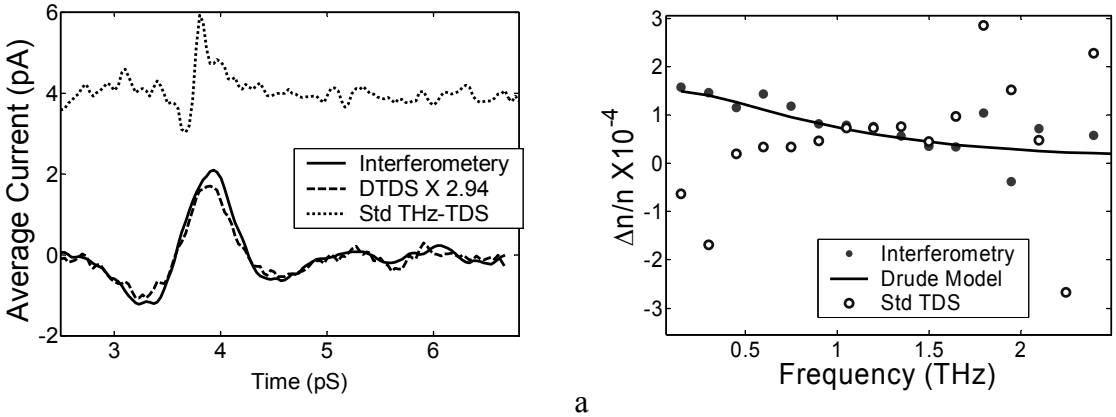

Figure 18. (a) THz pulses measured using THz interferometer (solid line), DTDS (dashed line), and the difference between two consecutive THz scans taken with and without optical excitation (dotted line). (b) Optically-induced change in refractive index determined from THz interferometry (dots), THz-TDS (open circles), and Drude theory (line).

Figure 18a compares the difference between two consecutive THz scans taken with and without optical excitation (dotted), a single data scan taken using DTDS (dashed), and a scan on the THz interferometer (solid) with the constant background signal numerically subtracted[16]. The DTDS scan has been normalized to the throughput of the THz interferometer (34.7%). The ratio between peak signal and background noise of the difference signal is 4.9:1. For the data scan using the THz interferometer the ratio is 21:1 while that of the DTDS measurement is 22:1.

Figure 18b plots the measured optically-induced change in refractive index, $\Delta n(\omega)/n(\omega)$, obtained from the THz interferogram (points) and that determined by THz-TDS (open circles), both using the Fourier transform of the temporal data of Figure 18a. The index change calculated according to Drude theory is shown as a solid line. The measured index change was determined taking into account the Fresnel transmission coefficients on the input and output faces of the Si wafer, but not the Fabry-Perot term since reflections from the wafer faces were time gated out[10]. Using THz interferometry, index changes of

one part in 10^{-4} can be measured, which corresponds to an optical path length change of 342nm. At unity signal to noise ratio ΔOPL reduces to 28nm.

Chapter 5

FUTURE DIRECTIONS

Fourier Optical Noise Filtering

As indicated earlier beam asymmetry could represent a fundamental limitation to the Michelson THz interferometers developed thus far owing to the likeliness of a residual signal regardless of alignment quality. Equation 22 holds in the case that the reference signal with each arm of the interferometer transmitting through matched blanks is null at the receiver. If beam asymmetry is indeed found to significantly contribute to the residual field found in current THz interferometers then the artifact can be treated as an additional uncorrelated noise source rather than combined into overall system drift.

One solution at reducing the effects of beam symmetry mismatch may be through the use of a Fourier optical spatial filter in which an aperture is placed after the first paraboloidal mirror where the beam is Fourier transformed to a frequency-dependent waist region. Aberrations in the untransformed quasi-Gaussian beam profile in the form of localized field peaks will spatially broaden in the transformed region, while the dominant quasi-Gaussian shape is retained under optical transformation. The aperture permits the latter and restricts the former and may improve the uniformity of the beam.

Spatial measurements of frequency amplitude and phase propagation of pulsed THz beams have been investigated and shown to exhibit Laguerre–Gaussian propagation with at least 20 radial and 5 angular superimposed modes[20]. Although due to the reduction of waist

size compared to Gaussian beam properties this must be taken into account when selecting a Fourier mask the spatial filtering approach remains viable. As the schematic of the experimental setup in Figure 15 shows, the aperture must be placed before the waist region due to obstruction of the instrument optics. Consideration of Laguerre–Gaussian propagation becomes essential to understanding the optimized aperture size. Experimentally, the interferometric reference signal should improve closer to zero with minimal degradation of overall signal.

THz Polarimetric Interferometer

An alternate solution is proposed here to alleviate the beam asymmetry problem through a newly designed THz interferometer. Unlike previous techniques in THz interferometry this configuration is based on *constructive* interference and the detection of polarization changes between input and output beams much like is done with polarimetric technique of ellipsometry. For this reason we will refer to this design as a THz polarimetric interferometer. The configuration employs wire grid polarizers as beam splitters often seen in Martin-Puplett interferometers used to measure small differences between two input signals[30]. The polarimetric interferometer differs from the Martin-Puplett design in that there is a single input beam, the splitting and recombining polarizers are independent and orthogonally oriented to one another, and there are no roof mirrors.

Similar to ellipsometry, which is based on the detection of polarization-sensitive interactions from a sample by either reflection from a surface or transmission through a thin film, in the polarimetric interferometer linearly polarized light undergoes amplitude or phase changes or both so that post-interaction light is polarized elliptically. One difference from

ellipsometry is that only a single polarization component interacts with the sample.

In the THz polarimetric interferometer the beams are separated into orthogonally polarized components, one passing through the sample and the other through a reference then recombined into an elliptically-polarized output pulse. The THz receiver measures the small difference between the components by taking advantage of its polarization sensitivity. With the polarimetric interferometer beam asymmetry is no longer a source of error because each arm of the interferometer undergoes the same number of π-phase shifts from mirror and wire-grid polarizer reflections, thus no symmetry mismatch arises. This is not achievable in the THz Michelson interferometer since the zero signal is designated by the full cancellation of a portion of each pulse with a π-shifted version of itself. Additionally, for a given input pulse, the field amplitudes measured by the polarimetric interferometer are expected to be larger than that of the Michelson interferometer by a factor on the order of 1.4 (See Appendix C).

A schematic of the polarimetric interferometer is shown in Figure 19. Pulses that are linearly polarized at 45° are collimated by off-axis paraboloidal mirror OAPM. A free-standing wire-grid polarizer P1 is oriented with wires at 45° which transmits electric fields oriented at -45°. This serves to filter any cross-polarization components that have arisen from off-axis illumination of the paraboloidal mirror[31]. The beam is then polarization-separated into orthogonal components by the second polarizer P2 having horizontally oriented wires. Horizontally polarized pulses reflect from the polarizer then travel to front-surface mirror M1, pass through sample S then reflect from another front-surface mirror M2.

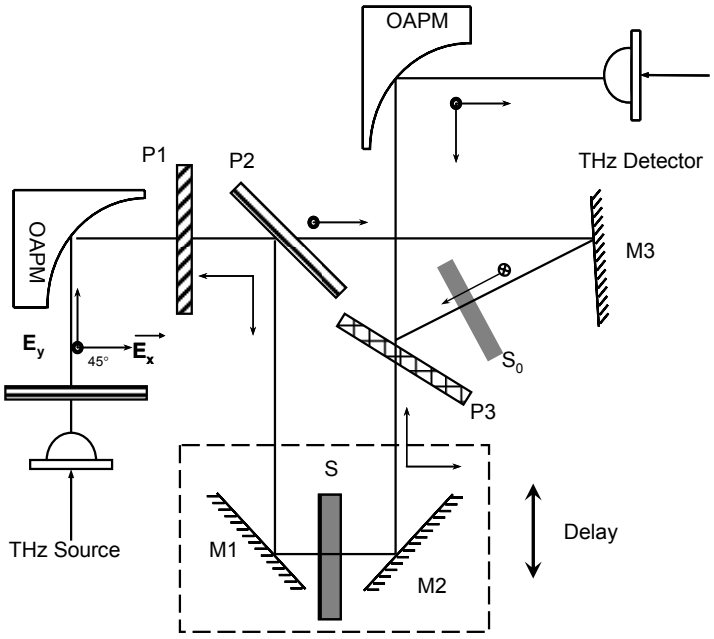

Figure 19. Polarimetric interferometer. Beam mismatch is alleviated by detection of polarization rotation rather than cancellation as with the Michelson interferometer. OAPM are off-axis paraboloidal mirrors. M1, M2 and M3 are front-surface mirrors. P1, P2 and P3 are 45°, horizontally and vertically oriented wire grid polarizers, respectively. S and S_o are sample and reference materials.

M1, S, and M2 are mounted on an adjustable platform to allow balancing the path length between each arm. Pulses with vertical polarization pass through polarizer P2 and reflect from a single front-surface mirror M3 and through reference medium S_o in a fixed-length path. The beams of each arm are *constructively* recombined at polarizer P3 having wires aligned vertically. Pulses from the sample arm transmit through P3 while those of the reference arm reflect. With the sample removed, after reflection from the final paraboloidal mirror the pulse is restored to the same state as at the input. No cross-polarization occurs because the beam is coaxially incident to the paraboloidal mirror[25]. The zero reference signal is achieved by orienting the detector, a plane-polarization sensitive device, orthogonally to the output polarization (-45° to horizontal). When a sample is then replaced the horizontally polarized pulses undergo a phase shift according to the optical properties of

the sample. Upon recombination with the reference pulses, the polarization plane rotates relative to the initial polarization plane. The detection axis of the receiver which had zero field in the reference case, now responds to the small component that must exist in the rotated output field.

One significant difference between the polarimetric and Michelson interferometers is the respective single-pass vs. double-pass sampling. The advantage of a double-pass is particular when dealing with thin media since small interaction lengths are the very source of difficulties in THz TDS measurements and the double-pass extends the interaction length by a factor of 2. On the other hand, in the case of highly absorptive media such as water, single-pass sampling would be preferable since field attenuation is so drastic.

In actuality reflection losses due to the single beam-splitter in the Michelson design reduce the measurement capabilities to a greater extent than does eliminating a sampling pass. To show this, a detailed field analysis of the polarimetric interferometer is referenced in Appendix C which verifies the measurement equivalence between it and the Michelson design. For the latter we find from eq. 20 that for film of thickness *d* the measured THz interferometric field $E_{meas}^{M}(\omega)$ is described by

$$E_{meas}^{M}(\omega)=\frac{1}{2}\left(e^{ik(\omega)2d}-e^{ik_0(\omega)2d}\right)E_i(\omega)\tilde{\kappa}(\omega) \qquad 39$$

where the parameter $\tilde{\kappa}(\omega)$ has been described in chapter 3. For the polarimetric interferometer the measurement is in fact

$$E_{meas}^{P}(\omega)=\frac{1}{2}\left(e^{ik(\omega)d}-e^{ik_0(\omega)d}\right)E_i(\omega) \qquad 40$$

It is further shown in Appendix C that

$$E_{meas}^{P}\cong 1.42E_{meas}^{M} \qquad 41$$

due primarily to the interface losses of the silicon beam splitter in the Michelson case. Nonetheless, the Michelson interferometer has been well characterized in this and previous work and shown to effective reduce random errors and noise associated with standard THz TDS measurements. However the many advantages of the polarimetric THz interferometer presented here provide ample justification for exploring the technique.

Biological Applications

The THz radiation band houses strong potential in non-destructive analysis of biological molecules owing to low energy content. Biomolecular samples were first examined with THz-TDS by measuring vibrational modes of calf thymus DNA, bovine serum albumin (BSA), and collagen [32]. The dynamical response of a solvent to a solute still remains a poorly understood but important scientific problem. A large number of important processes such as ion association, dissociation, transport, and charge transfer reactions occur in liquids, and all are significantly influenced by the solvent dynamics. A step towards understanding solvation dynamics is the determination of the dielectric response of pure solvents to far-infrared radiation, which probes molecular motions occurring on time scales of 1–10 ps. This can then be followed by the determination of the dielectric response of those same solvents when they are perturbed by electrolytes. Work has been done previously using time domain THz spectroscopy to characterize the dielectric properties of various solvents over large ranges of concentration, however resolution of small changes is difficult in this single-beam measurement [33]. THz time-domain interferometry has promising gain in revealing dielectric changes with small changes in ionic concentrations. Future work in this area may lead to interferometric measurements of biological molecular

dynamics in the aqueous environment, typically problematic in the IR region.

References

1. Siegel, R.W. *R&D Status and Trends in Nanoparticles, Nanostructured Materials, and Nanodevices in the United States*. in *WTEC Workshop*. 1997. Arlington, Virginia.
2. *Surface Engineering, Science and Technology I*. in *128th Annual Meeting & Exhibition of The Minerals, Metals & Materials Society*. 1999. San Diego, California.
3. Sprik, R., I.N. Duling, III, C.C. Chi, and D. Grischkowsky, *Far infrared spectroscopy with subpicosecond electrical pulses on transmission lines.* Applied Physics Letters, 1987. **51**(7): p. 548-50.
4. Katzenellenbogen, N. and D. Grischkowsky, *Efficient generation of 380 fs pulses of THz radiation by ultrafast laser pulse excitation of a biased metal- semiconductor interface.* Appl. Phys. Lett., 1991. **58**(3): p. 222-4.
5. Berger, L., *Semiconductor Materials*. 1997, Baca Raton: CRC Press.
6. Adachi, S. and N.T.T.C.M.J. Musashino Electr. Commun. Lab, *Gallium arsenide, aluminum arsenide, and aluminum gallium arsenide (AlxGa1-xAs): material parameters for use in research and device applications*. J. Appl. Phys., 1985. **58**(3): p. R1-R29.
7. Johnson, J.L., T.D. Dorney, D.M. Mittleman, Electrical, and R.U.H.T.X.U.S.A. Computer Engineering Department, *Enhanced depth resolution in terahertz imaging using phase-shift interferometry.* Appl. Phys. Lett., 2001. **78**(6): p. 835-837.
8. van Exter, M. and D.R. Grischkowsky, *Characterization of an optoelectronic terahertz beam system*. IEEE Trans. Microwave Theory Tech., 1990. **38**(11): p. 1684-91.

9. Procházka, A., *Signal analysis and prediction*. Applied and numerical harmonic analysis, ed. A. Procházka. 1998, Boston: Birkhauser.

10. Duvillaret, L., F. Garet, and J.-L. Coutaz, *Influence of noise on the characterization of materials by terahertz time-domain spectroscopy*. J. Opt. Soc. Am. B, 2000. **17**(3): p. 452-461.

11. Grischkowsky, D., S. Keiding, M. van Exter, and C. Fattinger, *Far-infrared time-domain spectroscopy with terahertz beams of dielectrics and semiconductors*. J. Opt. Soc. Am. B, 1990. **7**(10): p. 2006-15.

12. James D. Ingle, J. and S.R. Crouch, *Spectrochimical Analysis*. 1988, Upper Saddle River: rentice Hall. 590.

13. Lee, K.-S., T.-M. Lu, and X.-C. Zhang, *The measurement of the dielectric and optical properties of nano thin films by THz differential time-domain spectroscopy*. Microelectronics Journal, 2003. **34**: p. 63-69.

14. Jiang, Z., M. Li, and X.C. Zhang, *Dielectric constant measurement of thin films by differential time-domain spectroscopy*. Applied Physics Letters, 2000. **76**(22): p. 3221-3223.

15. M. Brucherseifer, P.H.B., and H. Kurz, *Combined optical and spatial modulation THz-spectroscopy for the analysis of thin-layered systems*. Applied Physics Letters, 2002. **81**(10): p. 1791-1793.

16. Krishnamurthy, S., M.T. Reiten, S.A. Harmon, and R.A. Cheville, *Characterization of thin polymer films using terahertz time-domain interferometry*. Applied Physics Letters, 2001. **79**(6): p. 875-877.

17. Small, J.A. and R.A. Cheville, *Measurement and noise characterization of optically induced index changes using THz interferometry*. Applied Physics Letters, 2004. **84**(21): p. 4328-4330.

18. Jon L. Johnson, T.D.D., Daniel M. Mittleman, *Interferometric Imaging With Terahertz Pulses*. Selected Topics in Quantum Electronics, 2001. **7**(4): p. 592-599.

19. Hecht, E., *Optics*. 2002, San Francisco: Addison Wesley.

20. Reiten, M.T., S.A. Harmon, and R.A. Cheville, *Terahertz beam propagation measured through three-dimensional amplitude profile determination.* J. Opt. Soc. Am. B, 2003. **20**(10).

21. Dekorsy, T., H. Auer, H.J. Bakker, H.G. Roskos, and H. Kurz, *THz electromagnetic emission by coherent infrared-active phonons.* Phys. Rev. B, 1996. **53**(7): p. 4005-4014.

22. Spielman, S., B. Parks, J. Orenstein, D.T. Nemeth, F. Ludwig, J. Clarke, P. Merchant, and D.J. Lew, *Observatin of the Quasiparticle Hall Effect in Superconducting YBa2 Cu3 O7-delta.* Phys. Rev. Lett., 1994. **73**(11): p. 1537-1540.

23. Wynne, K. and D.A. Jaroszynski, *Superluminal terahertz pulses.* Optics Letters, 1999. **24**(1): p. 25-27.

24. Rudd, J.V., J.L. Johnson, and D.L. Mittleman, *Quadruple radiation from terahertz dipole antennas.* Optics Letters, 2000. **25**(20): p. 1556-1558.

25. Jacobsen, J., *On the Cross Polarization of Asymmetric Reflector Antennas for Satellite Applications.* IEEE Trans on Antennas and Propagation, 1977. **25**(2): p. 276-283.

26. van Exter, M. and D. Grischkowsky, *Carrier dynamics of electrons and holes in moderately doped silicon.* Physical Review B (Condensed Matter), 1990. **41**(17): p. 12140-9.

27. Jeon, T.I. and D. Grischkowsky, *Nature of conduction in doped silicon.* Physical Review Letters, 1997. **78**(6): p. 1106-1109.

28. Sze, S.M., *Physics of Semiconductor Devices.* 1981: John Wiley and Sons, Inc. New York.

29. Brucherseifer, M., P.H. Bolivar, and H. Kurz, *Combined optical and spatial modulation THz-spectroscopy for the analysis of thin-layered systems.* Applied Physics Letters, 2002. **81**(10): p. 1791-1793.

30. Seizi Nishizawa, N.T., Hideaki Kitahara, Mitsuo Wada Takeda, Seiji Kojima, *New application of terahertz time-domain spetrometry (THz-TDS) to phonon-polariton observation on ferroelectric crystals.* Physics in Medicine and Biology, 2002. **47**(21): p. 3771-3776.

31. Gans, M.J., *Cross polarization in reflector type beam waveguides and antennas.* Bell Sys. Tech Jour., 1976. **55**(3): p. 289-316.

32. Markelz, A.G., A. Roitberg, E.J. Heilweil, and N.G.M.D.U.S.A. Optical Technology Division, *Pulsed terahertz spectroscopy of DNA, bovine serum albumin and collagen between 0.1 and 2.0 THz.* Chem. Phys. Lett., 2000. **320**(1,2): p. 42-48.

33. Asaki, M.L.T., A. Redondo, T.A. Zawodzinski, and A.J. Taylor, *Dielectric relaxation of electrolyte solutions using terahertz transmission spectroscopy.* The Journal of Chemical Physics, 2002. **116**(19): p. 8469-8482.

34. Mickan, S.P., K.-S. Lee, T.-M. Lu, J. Munch, D. Abbott, and X.-C. Zhang, *Double modulated differential THz-TDS for thin film dielectric characterization.* Microelectronics Journal, 2002. **33**: p. 1033-1042.

A p p e n d i x A

POLARIZATION OPERATORS

The value of polarization operator $\underset{\sim}{T}$ is obtained using the standard Jones operator matrices of the individual elements within the interferometer. They are defined in Table 1 below [19].

Optical Element	Jones Matrix Operator
$\underset{\sim}{R}_A$	$\begin{bmatrix} -1 & 0 \\ 0 & 1 \end{bmatrix}$
$\underset{\sim}{M}_1, \underset{\sim}{M}_2, \underset{\sim}{R}_B, \underset{\sim}{B}_r$	$\begin{bmatrix} 1 & 0 \\ 0 & -1 \end{bmatrix}$
$\underset{\sim}{B}_t$	$\begin{bmatrix} 1 & 0 \\ 0 & 1 \end{bmatrix}$
$\underset{\sim}{S}_0$	$\begin{bmatrix} e^{ik_0(\omega)2d} & 0 \\ 0 & e^{ik_0(\omega)2d} \end{bmatrix}$
$\underset{\sim}{S}$	$\begin{bmatrix} e^{ik(\omega)2d} & 0 \\ 0 & e^{ik(\omega)2d} \end{bmatrix}$
$\underset{\sim}{P}_1$	$\begin{bmatrix} 1 & 0 \\ 0 & 0 \end{bmatrix}$

Table 1. Jones Matrix operators of the optical elements of the Michelson interferometer

Using these in eq. 18 results in

$$\underset{\sim}{T} = \frac{1}{2}\begin{bmatrix} 1 & 0 \\ 0 & -1 \end{bmatrix}\left\{\begin{bmatrix} 1 & 0 \\ 0 & -1 \end{bmatrix}\begin{bmatrix} -1 & 0 \\ 0 & 1 \end{bmatrix}\begin{bmatrix} e^{ik_0(\omega)2d} & 0 \\ 0 & e^{ik_0(\omega)2d} \end{bmatrix}\begin{bmatrix} 1 & 0 \\ 0 & 1 \end{bmatrix} + \begin{bmatrix} 1 & 0 \\ 0 & 1 \end{bmatrix}\begin{bmatrix} 1 & 0 \\ 0 & -1 \end{bmatrix}\begin{bmatrix} e^{ik(\omega)2d} & 0 \\ 0 & e^{ik(\omega)2d} \end{bmatrix}\begin{bmatrix} 1 & 0 \\ 0 & -1 \end{bmatrix}\right\}\begin{bmatrix} 1 & 0 \\ 0 & 0 \end{bmatrix}\begin{bmatrix} 1 & 0 \\ 0 & -1 \end{bmatrix} \quad \text{A-1}$$

$$\underset{\sim}{T} = \frac{1}{2}\begin{bmatrix} e^{ik(\omega)2d} - e^{ik_0(\omega)2d} & 0 \\ 0 & 0 \end{bmatrix}. \quad \text{A-2}$$

Appendix B

MEASUREMENT OF RECOMBINATION TIME CONSTANT τ_r

The carrier lifetime τ_r was measured using double-modulated THz-DTDS[34]. The apparatus used corresponds to the DTDS measurements discussed in the section on Photo-induced Index Change. Because THz-DTDS measures the difference between the modulated indices if the illumination frequency is higher than $1/\tau_r$ photo-generated free carriers will not recombine in the Si slab during the dark phase of modulation before the next excitation phase begins. The difference in index between these two phases will tend to zero with increasing modulation frequency. When the frequency is less than $1/\tau_r$ however, the difference signal will attain its maximum value. The results of this measurement are shown in Figure 20.

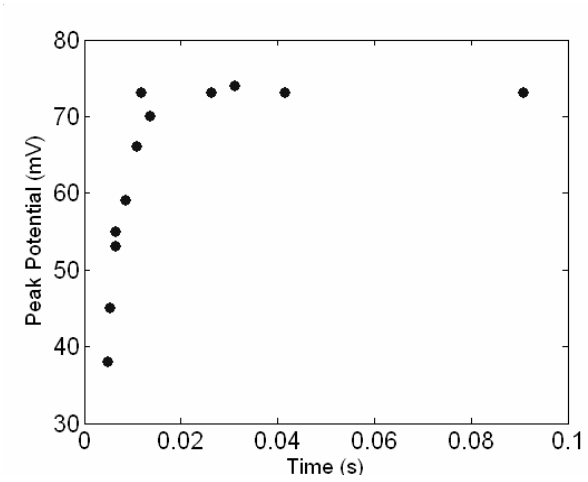

Figure 20. Data for measurement of recombination time τ_r. Maximum signal occurs at about 25ms.

A p p e n d i x C

FIELD ANALYSIS OF POLARIMETRIC INTERFEROMETER

To illustrate the measurement equivalence of the THz Michelson and polarimetric interferometers the electric field analysis for each configuration is compared. Chapter 2 saw the Jones development of the Michelson design with the final result of eq. 20 restated here:

$$\mathbf{E}_{out}(\omega) = \frac{1}{2}\left(e^{ik(\omega)2d} - e^{ik_0(\omega)2d}\right) E_i(\omega)\tilde{\boldsymbol{\kappa}}(\omega)\hat{\mathbf{x}}. \qquad \text{C-1}$$

This is the output field of the Michelson interferometer for purely horizontally-polarized input field. In the THz Michelson interferometer the receiver is oriented as to only detect *x*-component radiation. On the other hand, eq. C-1 indicates no field is expected elsewhere so

$$\mathbf{E}_{meas}(\omega) = \mathbf{E}_{out}(\omega). \qquad \text{C-2}$$

In the case of the polarimetric interferometer the input beam $\mathbf{E}_i(\omega)$ is polarized +45° relative to the horizontal so that

$$\mathbf{E}_i(\omega) = \frac{\sqrt{2}}{2}\begin{bmatrix}1\\1\end{bmatrix} E_i(\omega). \qquad \text{C-3}$$

Referring to

Figure 19 we calculate the output of the interferometer by

$$\mathbf{E}_{out}(\omega) = \left[\underset{\sim}{M}_{OAP}\left(\underset{\sim}{P}_{2t}\underset{\sim}{M}_3\underset{\sim}{S}_0\underset{\sim}{P}_{3r} + \underset{\sim}{P}_{2r}\underset{\sim}{M}_1\underset{\sim}{S}\underset{\sim}{M}_2\underset{\sim}{P}_{3t}\right)\underset{\sim}{P}_1\underset{\sim}{M}_{OAP}\right]\mathbf{E}_i(\omega)\tilde{\boldsymbol{\kappa}}(\omega) \qquad \text{C-4}$$

where $\underset{\sim}{M}_{OAP}$ is the Jones matrix for the off-axis paraboloidal mirror and $\underset{\sim}{M}_{1,2,3}$ are those of mirrors M_1, M_2, and M_3. $\underset{\sim}{P}_1$, $\underset{\sim}{P}_{2t}$, $\underset{\sim}{P}_{2r}$, $\underset{\sim}{P}_{3t}$, and $\underset{\sim}{P}_{3r}$ are the indicated polarizer operators according to transmission *t* or reflection *r*. The operators are tabulated in Table 2[19].

Optical Element	**Jones Matrix Operator**
$\underset{\sim}{M}_{OAP}, \underset{\sim}{M}_{1,2,3}, \underset{\sim}{P}_{2r}, \underset{\sim}{P}_{1r}$	$\begin{bmatrix} 1 & 0 \\ 0 & -1 \end{bmatrix}$
$\underset{\sim}{P}_1$	$\frac{1}{2}\begin{bmatrix} 1 & -1 \\ -1 & 1 \end{bmatrix}$
$\underset{\sim}{P}_{2t}$	$\begin{bmatrix} 0 & 0 \\ 0 & 1 \end{bmatrix}$
$\underset{\sim}{P}_{3t}$	$\begin{bmatrix} 1 & 0 \\ 0 & 0 \end{bmatrix}$
$\underset{\sim}{S}_0$	$\begin{bmatrix} e^{ik_o(\omega)d} & 0 \\ 0 & e^{ik_o(\omega)d} \end{bmatrix}$
$\underset{\sim}{S}$	$\begin{bmatrix} e^{ik(\omega)d} & 0 \\ 0 & e^{ik(\omega)d} \end{bmatrix}$

Table 2. Jones Matrix operators of the optical elements of the polarimetric interferometer.

Carrying out the computation of $\mathbf{E}_{out}(\omega)$ using eq. C-4 we find

$$\mathbf{E}_{out}(\omega) = \begin{bmatrix} 1 & 0 \\ 0 & -1 \end{bmatrix} \left\{ \begin{array}{c} \begin{bmatrix} 0 & 0 \\ 0 & 1 \end{bmatrix}\begin{bmatrix} 1 & 0 \\ 0 & -1 \end{bmatrix}\begin{bmatrix} e^{ik(\omega)d} & 0 \\ 0 & e^{ik(\omega)d} \end{bmatrix}\begin{bmatrix} 1 & 0 \\ 0 & -1 \end{bmatrix} \\ + \\ \begin{bmatrix} 1 & 0 \\ 0 & -1 \end{bmatrix}\begin{bmatrix} 1 & 0 \\ 0 & -1 \end{bmatrix}\begin{bmatrix} e^{ik_0(\omega)d} & 0 \\ 0 & e^{ik_0(\omega)d} \end{bmatrix}\begin{bmatrix} 1 & 0 \\ 0 & -1 \end{bmatrix}\begin{bmatrix} 1 & 0 \\ 0 & 0 \end{bmatrix} \end{array} \right\} \frac{1}{2}\begin{bmatrix} 1 & -1 \\ -1 & 1 \end{bmatrix}\begin{bmatrix} 1 & 0 \\ 0 & -1 \end{bmatrix}\mathbf{E}_i(\omega)$$

$$\mathbf{E}_{out}(\omega)=\begin{bmatrix} \frac{1}{2}e^{ik_0(\omega)d} & \frac{1}{2}e^{ik_0(\omega)d} \\ \frac{1}{2}e^{ik(\omega)d} & \frac{1}{2}e^{ik(\omega)d} \end{bmatrix}\mathbf{E}_i(\omega) \qquad \text{C-5}$$

Substituting for $\mathbf{E}_i(\omega)$ from eq. C-3:

$$\mathbf{E}_{out}(\omega)=\begin{bmatrix} \frac{1}{2}e^{ik_0(\omega)d} & \frac{1}{2}e^{ik_0(\omega)d} \\ \frac{1}{2}e^{ik(\omega)d} & \frac{1}{2}e^{ik(\omega)d} \end{bmatrix}\frac{\sqrt{2}}{2}\begin{bmatrix}1\\1\end{bmatrix}E_i(\omega) \qquad \text{C-6}$$

$$\mathbf{E}_{out}(\omega)=\frac{\sqrt{2}}{2}\begin{bmatrix} e^{ik_0(\omega)d} \\ e^{ik(\omega)d} \end{bmatrix}E_i(\omega). \qquad \text{C-7}$$

In the absence of a sample we have d=0 and we recover eq. C-3 ensuring that the input and output fields are identical when the interferometer is empty. Eq. C-7 establishes that the output field $\mathbf{E}_{out}(\omega)$ is linearly polarized +45° from horizontal. However, the THz detector is essentially a polarizer itself oriented at -45° and represented by P_D a -45° polarizer operator[19]

$$\underset{\sim}{P}_D=\frac{1}{2}\begin{bmatrix}1 & -1\\ -1 & 1\end{bmatrix}. \qquad \text{C-8}$$

Since it is arranged orthogonal to the incident field $\mathbf{E}_i(\omega)$ no net current is expected since carriers will not accelerate in the direction that will close the photoconductive switch. That is, for the fields along the detection axis of the THz receiver $\mathbf{E}_{meas}(\omega)$ we expect

$$\mathbf{E}_{meas}(\omega)=\underset{\sim}{P}_D\mathbf{E}_{out}(\omega)=0. \qquad \text{C-9}$$

This condition is seen more evidently by rotating the coordinate system of

$\mathbf{E}_{meas}(\omega)$ by $\pi/4$ relative to the input field so that the polarization is completely linear in $\hat{\mathbf{x}}'$ of the rotated frame. With the use of the rotation transformation matrix $\underset{\sim}{R}_{\vartheta}$ we have

$$\mathbf{E}_{meas}(\omega) = \underset{\sim}{R}_{\vartheta}\underset{\sim}{P}_{D}\mathbf{E}_{out}(\omega)$$

$$\mathbf{E}_{meas}(\omega) = \begin{bmatrix} \cos(\pi/4) & \sin(\pi/4) \\ -\sin(\pi/4) & \cos(\pi/4) \end{bmatrix} \frac{1}{2} \begin{bmatrix} 1 & -1 \\ -1 & 1 \end{bmatrix} \mathbf{E}_{out}(\omega)$$

$$\mathbf{E}_{meas}(\omega) = \frac{\sqrt{2}}{2} \begin{bmatrix} 0 & 0 \\ -1 & 1 \end{bmatrix} \mathbf{E}_{out}(\omega)$$

Substituting for $\mathbf{E}_{out}(\omega)$ from eq. C-7 gives

$$\mathbf{E}_{meas}(\omega) = \frac{\sqrt{2}}{2} \begin{bmatrix} 0 & 0 \\ -1 & 1 \end{bmatrix} \frac{\sqrt{2}}{2} \begin{bmatrix} e^{ik_0(\omega)d} \\ e^{ik(\omega)d} \end{bmatrix} E_i(\omega) \qquad \text{C-10}$$

$$\mathbf{E}_{meas}(\omega) = \frac{1}{2} \begin{bmatrix} 0 \\ e^{ik(\omega)d} - e^{ik_0(\omega)d} \end{bmatrix} E_i(\omega) \qquad \text{C-11}$$

And finally

$$\mathbf{E}_{meas}(\omega) = \frac{1}{2}\left(e^{ik(\omega)d} - e^{ik_0(\omega)d}\right) E_i(\omega)\hat{\mathbf{y}}' . \qquad \text{C-12}$$

which is identical in form to eq. C-1 for the Michelson interferometer but differs by factor

$$\tilde{\kappa}(\omega)\frac{e^{ik(\omega)2d} - e^{ik_0(\omega)2d}}{e^{ik(\omega)d} - e^{ik_0(\omega)d}} \qquad \text{C-13}$$

where we recall $\tilde{\kappa}(\omega)$ accounts for interface losses of the dielectric beam splitter of the Michelson interferometer and the difference in phase factor is due to single-pass vs. double-pass configurations of the polarimetric and Michelson interferometers, respectively. Eq. C-13 reduces further to

$$\tilde{\kappa}(\omega)\left(e^{ik(\omega)d}+e^{ik_0(\omega)2d}\right). \qquad \text{C-14}$$

The value of $\tilde{\kappa}(\omega)=0.35$ is evaluated in Appendix D and obtained from the Fresnel coefficients of Silicon. For thin samples of low refractive index the term in parentheses is very nearly equal to 2. From this we can conclude that the actual THz measurement of the polarimetric interferometer is still slightly larger than that of the Michelson interferometer despite the single-pass configuration:

$$\mathbf{E}_{Polarimetric} \cong 1.42\mathbf{E}_{Michelson} \qquad \text{C-15}$$

and is indifferent to asymmetries of the THz beam.

A p p e n d i x D

FRESNEL INTERFACE LOSS FACTOR $\tilde{\kappa}(\omega)$

The original signal undergoes reflection losses due to the silicon beam splitter which is essentially a dielectric slab with interface effects governed by the Fresnel relations[19]. Only one reflection pass is considered since the slab is thick enough to separate subsequent reflections out of the time domain of interest. Defining the air as medium 1 and the silicon slab as medium 2 we have the following Fresnel relations of import:

$$r_{12}(\omega) = \frac{n_1(\omega)\cos\theta - n_2(\omega)\cos\phi}{n_1(\omega)\cos\theta + n_2(\omega)\cos\phi} \qquad \text{D-1}$$

$$t_{12}(\omega) = \frac{2n_1(\omega)\cos\theta}{n_1(\omega)\cos\theta + n_2(\omega)\cos\phi} \qquad \text{D-2}$$

$$t_{21}(\omega) = \frac{2n_2(\omega)\cos\theta}{n_2(\omega)\cos\theta + n_1(\omega)\cos\phi} \qquad \text{D-3}$$

where in each relation θ is the angle of incidence from the first medium to the second medium and ϕ the angle of the transmitted wave in the second medium. For example, in eq. D-2 the first medium is medium air and the second is silicon while in eq. D-3 the first medium is silicon and the second is air.

The fraction of signal that passes through each arm A the interferometer is $r_{12}t_{12}t_{21}$ while that of arm B is $t_{12}t_{21}r_{12}$. Obviously $r_{12}t_{12}t_{21} = t_{12}t_{21}r_{12}$ and for

compactness we define

$$\tilde{\kappa}(\omega) \equiv r_{12}t_{12}t_{21} = t_{12}t_{21}r_{12} \qquad \text{D-4}$$

The complex nature of $\tilde{\kappa}(\omega)$ arises from any complex contribution of $n_1(\omega)$ or $n_2(\omega)$. For the silicon beam splitter there is negligible absorption at the bandwidth of interest, therefore $\tilde{\kappa}(\omega)$ will reduce to a real value in this case. However the complex notation of $\tilde{\kappa}(\omega)$ is retained for completeness. We have from eq.s D-1 through D-3

$$\begin{aligned} r_{12} &= 0.424 \\ t_{12} &= 0.416 \\ t_{21} &= 1.971 \end{aligned} \qquad \text{D-5}$$

from which eq. D-4 gives

$$\tilde{\kappa}(\omega) = 0.348\,. \qquad \text{D-6}$$

A p p e n d i x E

OPTICAL PATH INCREASE AS A FUNCTION OF DISPLACEMENT ANGLE OF A DIELECTRIC SLAB IN AIR

For a dielectric slab of thickness *d* and constant refractive index *n* suspended in air we wish to obtain the function $D(\theta)$ describing the increase in optical path length vs. displacement angle θ. Referring to Figure 21 the slab is initially at $\theta_0 = 0$. At some rotated angle θ_i the new path through the slab L is

$$L(\theta_i) = \frac{d}{\cos\left(\theta_t^{\theta_i}\right)} \qquad \text{E-1}$$

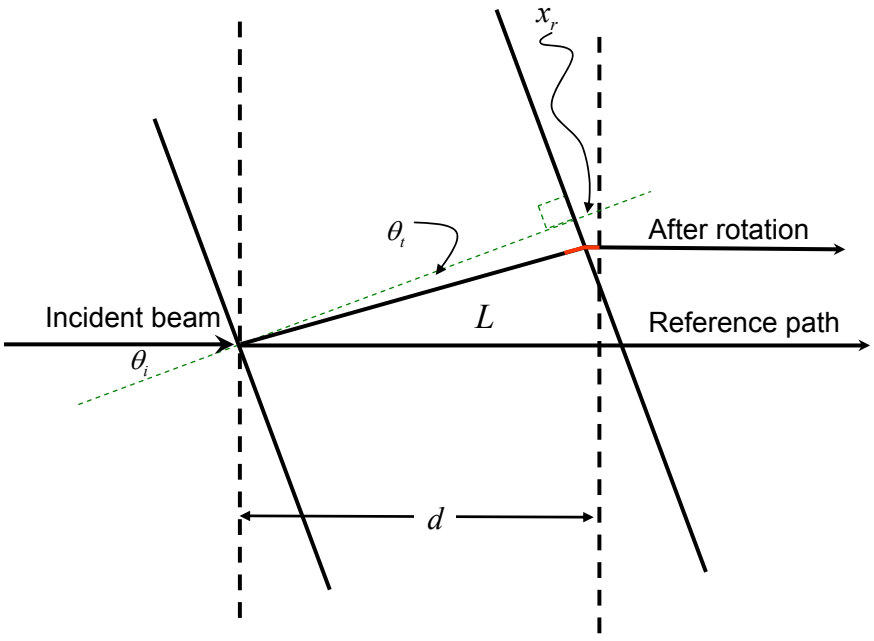

Figure 21. Schematic of a beam passing through a dielectric slab in air.

where the θ_i in $\theta_t^{\theta_i}$ denotes the θ_i dependency of θ_t according to Snell's law as

$$\theta_t^{\theta_i} = \sin^{-1}\left(\frac{\sin(\theta_i)}{n}\right). \quad \text{E-2}$$

The superscript notation has been employed for readability. An additional distance

$$x_r(\theta_i) = d - L(\theta_i)\cos\left(\theta_i - \theta_t^{\theta_i}\right) \quad \text{E-3}$$

propagated in air in the rotated configuration compared to the initial position indicated with the dashed lines adds to the total time delay due to the slab tilt. Because the total time delay is due to $(L-d)n/c$ through the slab plus x_r/c through air we must keep the description of the measurement as a total phase difference $k\left(L(\theta)-d\right)+k_0 x_r(\theta)$. Strictly speaking THz interferometery measures only total phase difference between the arms. In the case where all phase difference occurs within a single medium this translates directly into material thickness. Since the total phase difference for the tilted slab measurements arise from two medium the only meaningful representation of the data is the difference between optical path. Understanding this we define the function $D(\theta_i)$ the optical path difference as a function of incident angle as

$$D(\theta_i) = \left[\left(L(\theta_i)-d\right)n + x_r(\theta_i)\right] \quad \text{E-4}$$

which with E-1 and E-3 reduce to

$$D(\theta_i) = \left[\left(\frac{d}{\cos\left(\theta_t^{\theta_i}\right)} - d\right)n + d - \left(\frac{d}{\cos\left(\theta_t^{\theta_i}\right)}\right)\cos\left(\theta_i - \theta_t^{\theta_i}\right)\right] \quad \text{E-5}$$

$$D(\theta_i) = d\left[\frac{n}{\cos\left(\theta_t^{\theta_i}\right)} - n + 1 - \left(\frac{\cos\left(\theta_i - \theta_t^{\theta_i}\right)}{\cos\left(\theta_t^{\theta_i}\right)}\right)\right] \quad \text{E-6}$$

Equation E-6 represents the absolute optical path length for a given angle of incidence

upon a dielectric slab. The optical path length change ΔL_{OP} between two different incident angles θ_1 and θ_2 is obtained by

$$\Delta L_{OP} = D(\theta_2) - D(\theta_1) \tag{E-7}$$

and with some algebra we can write:

$$\Delta L_{OP}(\theta_1, \theta_2, d) = \frac{d}{\cos\left(\theta_{t2}^{\theta_2}\right)\cos\left(\theta_{t1}^{\theta_1}\right)}\left[\begin{array}{c} n\left(\cos\left(\theta_{t2}^{\theta_2}\right) - \cos\left(\theta_{t1}^{\theta_1}\right)\right) - \cos\left(\theta_{t2}^{\theta_2}\right)\cos\left(\theta_{t1}^{\theta_1} - \theta_1\right) \\ + \cos\left(\theta_{t1}^{\theta_1}\right)\cos\left(\theta_2 - \theta_{t2}^{\theta_2}\right) \end{array}\right]. \tag{E-8}$$

VITA

Jay Austin Small

Candidate for the Degree of

Master of Science

Thesis: NOISE REDUCTION IN THZ-TDS DIELECTRIC CHARACTERIZATION OF THIN FILMS WITH THZ INTERFEROMETRY

Major Field: Photonics

Biographical:

Personal Data: Born in Port Arthur, Texas, on June 24, 1966, the son of Richly R. Hirsch and Rebecca E. Small.

Education: Graduated from Edmond Memorial High School, Edmond, Oklahoma in May 1984; received Bachelor of Science degree in Physics from Central State University in May 1997. Completed requirements for the Master of Science degree with a major in Photonics at Oklahoma State University in December, 2004.

Experience: Employed as a professional computer programmer in Oklahoma from 1987 to 2001 with companies including C.L. Frates & Co., Hadson Energy Resources, Tarby, Inc., and Blue Cross Blue Shield of Oklahoma.